nature neuroscience

ARTICLES

https://doi.org/10.1038/s41593-019-0419-y

Sensory lesioning induces microglial synapse elimination via ADAM10 and fractalkine signaling

Georgia Gunner[1], Lucas Cheadle[2,9], Kasey M. Johnson[1,9], Pinar Ayata[3,4], Ana Badimon[3], Erica Mondo[1], M. Aurel Nagy[2], Liwang Liu[1], Shane M. Bemiller[5], Ki-Wook Kim[6], Sergio A. Lira[7], Bruce T. Lamb[5], Andrew R. Tapper[1], Richard M. Ransohoff[8], Michael E. Greenberg[2], Anne Schaefer[3,4] and Dorothy P. Schafer[1*]

Microglia rapidly respond to changes in neural activity and inflammation to regulate synaptic connectivity. The extracellular signals, particularly neuron-derived molecules, that drive these microglial functions at synapses remain a key open question. Here we show that whisker lesioning, known to dampen cortical activity, induces microglia-mediated synapse elimination. This synapse elimination is dependent on signaling by CX3CR1, the receptor for microglial fractalkine (also known as CXCL1), but not complement receptor 3. Furthermore, mice deficient in CX3CL1 have profound defects in synapse elimination. Single-cell RNA sequencing revealed that *Cx3cl1* is derived from cortical neurons, and ADAM10, a metalloprotease that cleaves CX3CL1 into a secreted form, is upregulated specifically in layer IV neurons and in microglia following whisker lesioning. Finally, inhibition of ADAM10 phenocopies *Cx3cr1*$^{-/-}$ and *Cx3cl1*$^{-/-}$ synapse elimination defects. Together, these results identify neuron-to-microglia signaling necessary for cortical synaptic remodeling and reveal that context-dependent immune mechanisms are utilized to remodel synapses in the mammalian brain.

Microglia are resident CNS macrophages that are becoming increasingly appreciated as dynamic regulators of synaptic connectivity. This includes developmental synaptic pruning, whereby microglia are 'listening' to neural activity and engulfing synapses from less active neurons[1,2]. Mechanisms regulating this process of activity-dependent, microglial synapse elimination have largely focused on surface receptors expressed by microglia. Whether there are activity-dependent neuronal cues that instruct microglia to eliminate synapses remains an open question. The importance of elucidating these mechanisms is further emphasized in a large array of neurological disorders, including neurodegenerative diseases, for which dysregulated microglia-mediated synapse elimination has now been implicated[3].

Two of the major molecular pathways identified to modulate microglia function at synapses are phagocytic signaling through complement receptor 3 (CR3; also known as CD11b) and chemokine signaling through the fractalkine receptor CX3CR1. In the developing mouse visual thalamus, the complement proteins C3 and C1q localize to synapses, and microglia engulf synapses via CR3 expressed by microglia[2,4]. Blocking this synaptic engulfment in C3-, C1q-, or CR3-deficient mice results in sustained synaptic pruning defects. A similar molecular mechanism also appears to regulate early synapse loss in mouse models of neurodegeneration[5–7]. CX3CR1 is a G protein-coupled chemokine receptor that is highly enriched in microglia[8–10]. While CR3-dependent phagocytic signaling regulates synaptic pruning in the developing visual system, studies have demonstrated that these effects are independent of CX3CR1 (refs. [11,12]). Instead, in the developing hippocampus and barrel cortex, CX3CR1-deficient mice exhibit a transient delay in microglial recruitment to synapse-dense brain regions and a concomitant delay in the functional maturation of synapses[13,14]. Long term, CX3CR1-deficient mice demonstrate defects in social interactions and functional synaptic connectivity[15]. It is less clear how CX3CR1 is exerting these effects, and the relative involvement of the canonical CX3CR1 ligand fractalkine (CX3CL1) is unknown.

Here, we used the mouse barrel cortex system to identify activity-dependent mechanisms by which neurons communicate with microglia to regulate synapse remodeling. Sensory endings from trigeminal neurons transmit sensory information from the whisker follicles on the snout to the brainstem, then to the ventral posteromedial (VPM) nucleus of the thalamus. VPM neurons then project and form thalamocortical (TC) synapses largely within layer IV of the barrel cortex. These TC synapses form a highly precise topographic map in which each individual whisker is represented in the barrel cortex by a discrete bundle of TC synapses (that is, barrels) separated by septa[16]. This is a particularly powerful system for studying synapse remodeling, as TC synapses are highly sensitive to whisker manipulation, and removal of the whiskers results in dampened activity in the barrel cortex and elimination of TC synapses[17–23]. Despite a clear role for neural activity, the mechanism (or mechanisms) by which changes in activity elicit TC synapse remodeling is an open question.

We used whisker cauterization and trimming in postnatal mice, paradigms known to reduce activity in the corresponding

[1]Department of Neurobiology, Brudnick Neuropsychiatric Research Institute, University of Massachusetts Medical School, Worcester, MA, USA. [2]Department of Neurobiology, Harvard Medical School, Boston, MA, USA. [3]Fishberg Department of Neuroscience, Department of Psychiatry, Friedman Brain Institute, Icahn School of Medicine at Mount Sinai, New York, NY, USA. [4]Ronald M. Loeb Center for Alzheimer's Disease, Icahn School of Medicine at Mount Sinai, New York, NY, USA. [5]Stark Neurosciences Research Institute, Indiana University, Indianapolis, IN, USA. [6]Department of Pharmacology and Center for Stem Cell and Regenerative Medicine, University of Illinois College of Medicine, Chicago, IL, USA. [7]Precision Immunology Institute, Icahn School of Medicine at Mount Sinai, New York, NY, USA. [8]Third Rock Ventures, Boston, MA, USA. [9]These authors contributed equally: Lucas Cheadle, Kasey M. Johnson. *e-mail: Dorothy.schafer@umassmed.edu

barrel cortex[17–22]. We identify synapse elimination within 1 week of whisker removal and robust microglia-mediated synaptic engulfment. Unlike the developing visual system[2], synapse elimination in the barrel cortex is CR3-independent. Instead, we identify profound defects in TC synapse elimination in mice deficient in either CX3CR1 enriched in microglia or its ligand CX3CL1. Using single-cell RNA sequencing (RNA-seq), we further uncover that *Cx3cl1* is enriched in cortical neurons and that expression of *Adam10*, a metalloprotease known to cleave CX3CL1 into a secreted form, is increased specifically in layer IV neurons and microglia following sensory lesioning. Strikingly, pharmacological inhibition of ADAM10 phenocopies synapse elimination defects observed in CX3CL1- and CX3CR1-deficient mice. Together, these data provide new insight into activity-dependent molecular mechanisms by which neurons communicate with microglia. Our single-cell RNA-seq results further provide an unbiased approach to identify novel mechanisms underlying intercellular communication in response to sensory perturbations.

Results

Whisker lesioning induces rapid and robust elimination of TC inputs in the barrel cortex. To interrogate neuron–microglia signaling during synapse remodeling, we performed two different manipulations in separate cohorts of postnatal day 4 (P4) mice: unilateral whisker trimming and unilateral whisker lesioning by cauterization (Fig. 1; Supplementary Fig. 1a,b). These paradigms are known to reduce activity in the barrel cortex and maximize robust TC remodeling in the neonate while avoiding the critical window (P0–P3) when sensory loss disrupts initial TC input wiring and can induce neuronal apoptosis[24]. Also, each model has its own internal control, as the whiskers are left intact on the other side of the snout. Using antivesicular glutamate transporter 2 (VGluT2) immunostaining, we observed a decrease in TC presynaptic terminals within layer IV of the barrel cortex by 17 days after the beginning of whisker trimming (Supplementary Fig. 1a,b). These results are consistent with previous work showing decreased TC inputs within the barrel cortex following whisker trimming in neonates and adults[20,21,23]. This decrease in presynaptic terminals was accelerated in the whisker lesioning model. Within 6 days post-lesioning, VGluT2 immunoreactivity was decreased by ~75% in the deprived barrel cortex compared with the control barrel cortex within the same animal (Fig. 1b,c). This effect was not due to a downregulation of VGluT2, as we observed similar effects in mice that express a fluorescent reporter in thalamic neurons and their cortical projections (SERT-Cre;*Rosa26*$^{LSL.TdTomato/+}$ mice) (Supplementary Fig. 1c,d). Note, however, that in these mice, presynaptic terminals and axons are labeled with tdTomato as well as other cortical projections, which results in less robust detection of TC input elimination.

To exclude the possibility that TC input elimination induced by whisker lesioning was due to neuronal damage and loss, we also assessed cell death, injury-induced axon degeneration, and cell stress. We observed no significant increase in cleaved caspase 3$^+$ neurons or amyloid precursor protein (APP) accumulation in axons within the barrel cortex circuit following whisker removal (Supplementary Fig. 2d–f). However, an increase in the stress marker ATF3 was observed in trigeminal neurons (Supplementary Fig. 2a,b), but not in cortical or VPM neurons (Supplementary Fig. 2c). To further characterize molecular changes, we performed bulk RNA-seq of the barrel cortex following whisker lesioning. Consistent with the observed decreased activity in the barrel cortex, immediate-early genes such as *Fos* and genes related to neurotransmitter signaling were decreased in the deprived barrel cortex, with no change in genes related to cell stress or death 24 h post-lesioning (Fig. 1d–f). Instead, there was an increase in genes related to axon growth and phagocytic signaling. These data are most consistent with synapse loss, and possibly axonal remodeling, resulting from decreased neural activity. Given the robust presynaptic terminal loss elicited in the absence of significant neuronal cell death or degeneration, we used whisker cauterization-induced sensory lesioning in P4 mice as a model to dampen cortical activity for the remainder of the study.

Whisker lesioning induces microglial engulfment of TC inputs within the barrel cortex independent of CR3. In the visual system, microglia engulf and remove synapses in response to dampened neural activity[2,25,26]. Therefore, we next explored whether microglia similarly engulf and eliminate TC synaptic inputs in the barrel cortex following whisker lesioning. Microglia were labeled using a transgenic mouse that expresses enhanced green fluorescent protein (EGFP) under the control of the fractalkine receptor (*Cx3cr1*$^{EGFP/+}$ mice)[9], and TC presynaptic terminals were labeled using anti-VGluT2. Using fluorescent confocal microscopy and structured illumination microscopy, we detected an approximately twofold increase in the volume of engulfed TC inputs within microglia in the deprived barrel cortex within 24 h of removing the whiskers (Fig. 1g–o; Supplementary Fig. 3a). These inputs were largely localized within the microglia, but not yet significantly associated with lysosomes (Fig. 1g–i,l,m). At 5 days post-whisker removal, microglia had a more phagocytic morphology, with a more rounded and enlarged soma, and most engulfed TC inputs were completely localized within microglial lysosomes (Fig. 1k,n,o). In contrast, minimal TC inputs were detected within microglia in the control barrel cortex of the same animal at any time point assessed (Fig. 1h,j). In addition, the percentage of highly phagocytic microglia (phagocytic index >1% at 24 h and >2% at 5 days) was increased in the deprived cortex (Supplementary Fig. 3), which may reflect microglial heterogeneity or the limitations of using static imaging to capture a dynamic process. This increase in phagocytic activity was further reflected in our RNA-seq data (Fig. 1d–f). These data provide evidence to indicate that microglia engulf and eliminate TC inputs in the cortex several synapses away from a peripheral sensory lesion known to reduce activity in the cortex.

Complement-dependent phagocytic signaling is one of the best-characterized mechanisms by which microglia engulf and remodel synapses. During synaptic pruning in the developing mouse visual system, the complement proteins C1q and C3 localize to synapses[4]. Microglia subsequently engulf and eliminate these synapses via the microglial phagocytic receptor CR3 (ref. [2]). To determine whether this pathway also regulates microglia-mediated synapse elimination in the barrel cortex following whisker lesioning, we assessed microglial engulfment and elimination of TC inputs in CR3-deficient (CR3-KO) mice. Surprisingly, similar to wild-type mice, TC inputs were eliminated by 6 days post-whisker removal in CR3-KO mice (Supplementary Fig. 4a–c), and engulfed TC inputs were still detected within CR3-KO microglia in the deprived barrel cortex (Supplementary Fig. 4d–f). Together, these data demonstrate that CR3 is dispensable for sensory lesion-induced microglial engulfment and elimination of TC synapses in the barrel cortex.

CX3CR1-deficient mice have profound defects in structural and functional synapse remodeling following whisker lesioning. Besides CR3, the fractalkine receptor CX3CR1, a G protein-coupled chemokine receptor highly enriched in microglia, has also been implicated in regulating microglial function at developing synapses[13–15]. We therefore sought to assess whisker lesion-induced TC synapse remodeling in *Cx3cr1*$^{-/-}$ mice. Remarkably, unlike CR3-KO mice (Supplementary Fig. 4), elimination of VGluT2$^+$ TC presynaptic inputs and structural synapses (colocalized presynaptic VGluT2 and postsynaptic Homer puncta) 6 days post-whisker removal was completely blocked in *Cx3cr1*$^{-/-}$ mice compared with *Cx3cr1*$^{+/-}$ or *Cx3cr1*$^{+/+}$ littermates (Fig. 2). This was largely a presynaptic effect, as the density of postsynaptic Homer was unaffected,

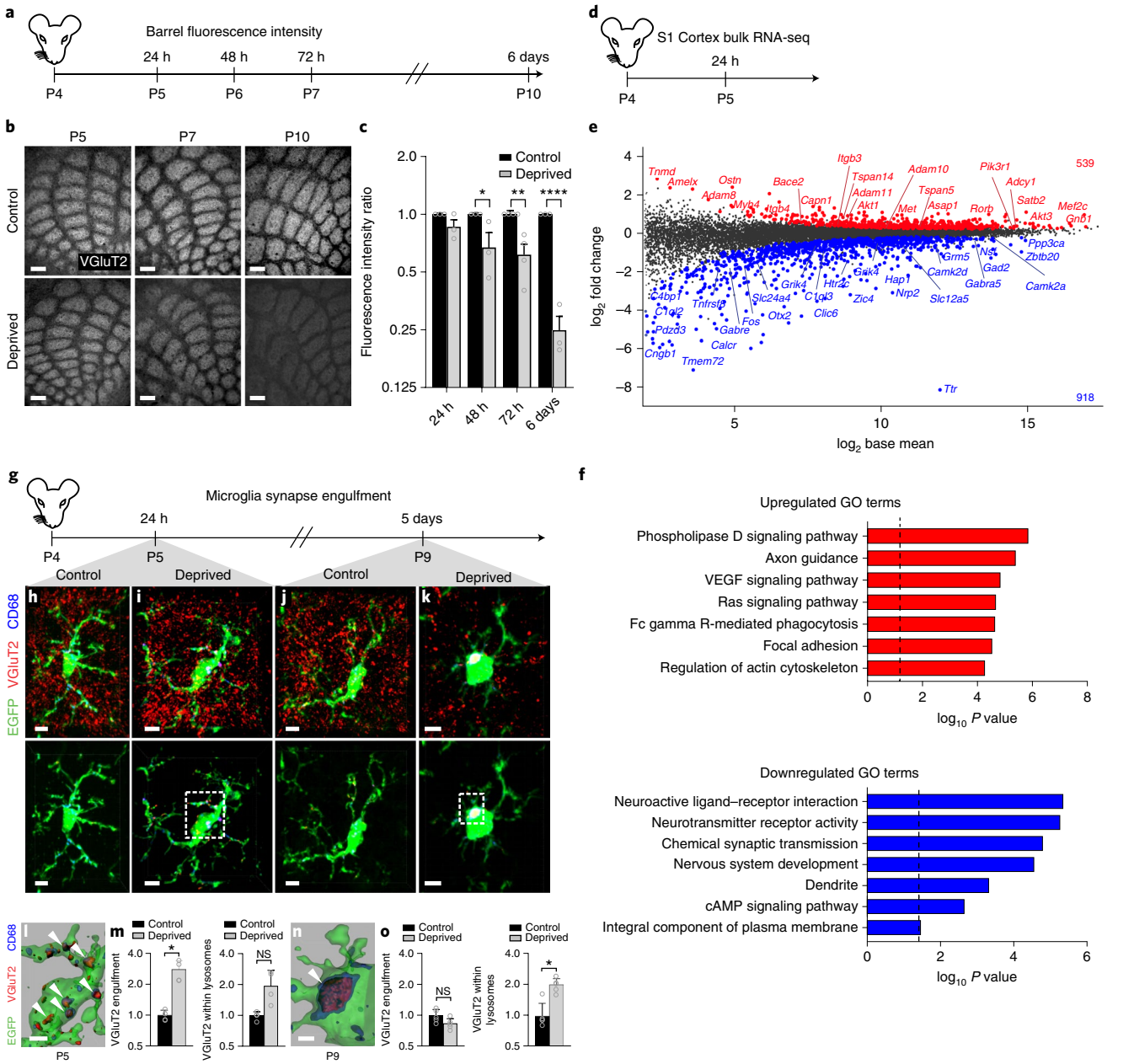

Fig. 1 | Whisker lesioning induces microglial engulfment and elimination of TC inputs within the barrel cortex. a, Timeline for analysis of TC input elimination following whisker lesioning at P4. **b**, Tangential sections of layer IV contralateral control (top) and deprived (bottom) barrel cortices immunolabeled for anti-VGluT2 show a decrease in TC inputs by P10. Scale bars, 150 µm. **c**, Quantification of fluorescence intensity of VGluT2$^+$ TC inputs in the barrel cortex in the deprived compared with the control barrel cortex at each time point post-whisker removal. Data normalized to the control, non-deprived hemisphere within each animal. Two-way ANOVA with Sidak's post hoc test; control versus deprived at 24 h, $n=3$ animals, $P=0.5323$, $t=1.419$, d.f. = 18; control versus deprived at 48 h, $n=3$ animals, $^*P=0.0142$, $t=3.349$, d.f. = 18; control versus deprived at 72 h, $n=4$ animals, $^{**}P=0.0011$, $t=4.516$, d.f. = 18; control versus deprived at 6 days, $n=3$ animals, $^{****}P<0.0001$, $t=7.631$, d.f. = 18. **d**, Timeline for bulk RNA-seq of the barrel cortex 24 h after whisker lesioning. **e**, MA plot (representing log-ratio (M) on the *y* axis and mean average (A) on the *x* axis) shows gene-expression changes (red, 539 upregulated genes; blue, 918 downregulated genes) in the deprived somatosensory cortex at P4 (DESeq2, $n=5$ mice, P5). **f**, Selected gene ontology (GO) annotations (Enrichr) enriched for upregulated or downregulated genes; dotted lines indicate $P=0.05$. **g**, Timeline for analysis of TC input engulfment by microglia. **h**–**k**, Fluorescent images of microglia (green) within layer IV of the control (**h** and **j**) and deprived (**i** and **k**) barrel cortices 24 h (**h** and **i**) and 5 days (**j** and **k**) after unilateral whisker removal. Microglial lysosomes are labeled with anti-CD68 (blue). Top: raw fluorescent images; bottom: VGluT2 signal internalized within microglia. Scale bars, 5 µm. **l**,**n**, The 3D surface-rendered images of the boxed areas of **i** and **k** (bottom). Arrowheads depict VGluT2 (red) internalized within microglia (green) and within lysosomes (blue). Scale bars, 2 µm. **m**,**o**, Quantification of VGluT2 engulfment within microglia (left) and VGluT2 engulfment within lysosomes (right) 24 h (**m**; within microglia: two-sided Student's *t*-test, $n=4$ animals, $^*P=0.0305$, $t=2.642$ d.f. = 6; within lysosomes: two-sided Student's *t*-test, $n=4$ animals, $P=0.2955$, $t=1.146$, d.f. = 6) and 5 days (**o**; within microglia: two-sided Student's *t*-test, $n=5$ animals, $P=0.3319$, $t=1.033$, d.f. = 8; within lysosomes: two-sided Student's *t*-test, $n=5$ animals, $^*P=0.0272$, $t=2.251$, d.f. = 8) after whisker removal in *Cx3cr1*$^{EGFP/+}$ microglia reveals increased VGluT2 within microglia at 24 h (**m**) and increased VGluT2 within microglial lysosomes at 5 days post-whisker removal (**o**). Data normalized to engulfment in microglia in the control hemisphere within each animal. All data are presented as the mean ± s.e.m.; NS, not significant.

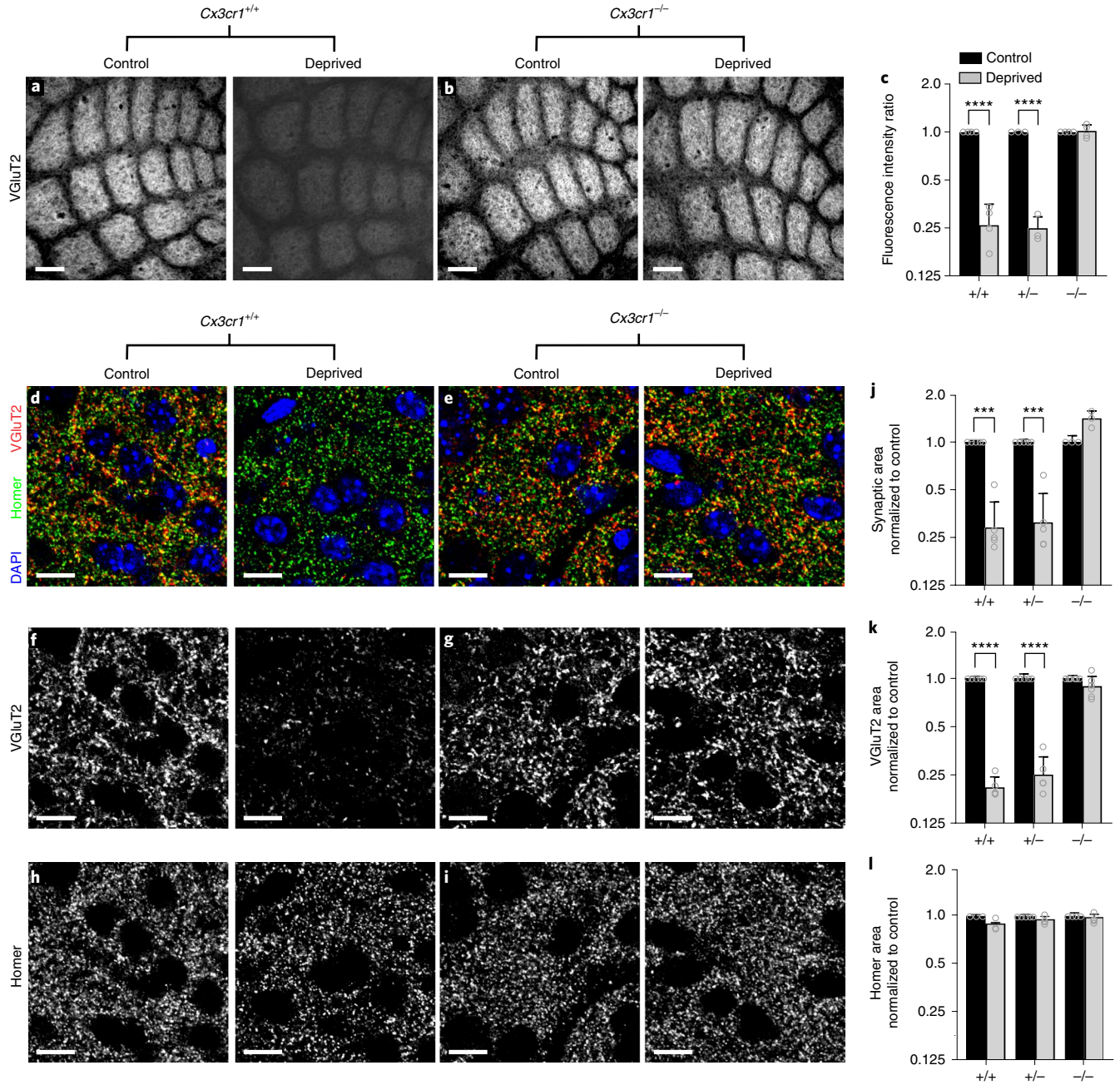

Fig. 2 | CX3CR1 is necessary for TC input elimination after whisker lesioning. a,**b**, VGluT2-immunolabeled TC inputs within tangential sections of control and deprived barrel cortices in *Cx3cr1*$^{+/+}$ (**a**) and *Cx3cr1*$^{-/-}$ mice (**b**) show TC inputs remain 6 days post-deprivation. Scale bars, 150 µm. **c**, Quantification of fluorescence intensity of VGluT2^{+} TC input immunoreactivity 6 days after deprivation in *Cx3cr1*$^{+/+}$, *Cx3cr1*$^{+/-}$, and *Cx3cr1*$^{-/-}$ littermates demonstrates a significant decrease in VGluT2 immunoreactivity in *Cx3cr1*$^{+/+}$ and *Cx3cr1*$^{+/-}$ mice following deprivation, but this is blocked in *Cx3cr1*$^{-/-}$ littermates. Data normalized to the control, non-deprived hemisphere within each animal. Two-way ANOVA with Sidak's post hoc test; control versus deprived *Cx3cr1*$^{+/+}$, $n=4$ animals, $^{****}P<0.0001$, $t=8.967$, d.f. = 16; control versus deprived *Cx3cr1*$^{+/-}$, $n=3$ animals, $^{****}P<0.0001$, $t=7.882$, d.f. = 16; control versus deprived *Cx3cr1*$^{-/-}$, $n=4$ animals, $P=0.9976$, $t=0.1722$, d.f. = 16. **d**–**i**, High-magnification (×63) confocal images of TC synapses within layer IV of the control and deprived barrel cortices immunolabeled with presynaptic anti-VGluT2 (red) and postsynaptic anti-Homer (green) 6 days post-deprivation in *Cx3cr1*$^{+/+}$ (**d**, **f**, and **h**) and *Cx3cr1*$^{-/-}$ (**e**, **g**, and **i**) mice. Merged channels are shown in **d** and **e**. The presynaptic VGluT2 channel alone is shown in **f** and **g**. The postsynaptic Homer channel alone is shown in **h** and **i**. Scale bars, 10 µm. **j**–**l**, Quantification of **d**–**i** reveals a significant decrease in structural synapses (**j**; colocalized VGluT2 and Homer, two-way ANOVA with Sidak's post hoc test, control versus deprived *Cx3cr1*$^{+/+}$, $n=5$ animals, $^{***}P=0.0004$, $t=4.765$, d.f. = 20; control versus deprived *Cx3cr1*$^{+/-}$, $n=5$ animals, $^{***}P=0.0005$, $t=4.617$, d.f. = 20; control versus deprived *Cx3cr1*$^{-/-}$ $n=3$ animals, $P=0.1290$, $t=2.139$, d.f. = 20) and VGluT2^{+} TC presynaptic terminal density (**k**; VGlut2 area, two-way ANOVA with Sidak's post hoc test, control versus deprived *Cx3cr1*$^{+/+}$, $n=5$ animals, $^{****}P<0.0001$, $t=6.919$, d.f. = 26; control versus deprived *Cx3cr1*$^{+/-}$, $n=5$ animals, $^{****}P<0.0001$, $t=6.552$, d.f. = 26; control versus deprived *Cx3cr1*$^{-/-}$, $n=6$ animals, $P=0.6907$, $t=1.006$, d.f. = 26) in *Cx3cr1*$^{+/+}$ and *Cx3cr1*$^{+/-}$ mice, which was blocked in *Cx3cr1*$^{-/-}$ littermates. There was no significant change in postsynaptic Homer density (**l**; Homer area, two-way ANOVA with Sidak's post hoc test, control versus deprived *Cx3cr1*$^{+/+}$, $n=3$ animals, $P=0.2386$, $t=1.811$, d.f. = 18; control versus deprived *Cx3cr1*$^{+/-}$, $n=5$ animals, $P=0.7852$, $t=0.9918$, d.f. = 18; control versus deprived *Cx3cr1*$^{-/-}$, $n=4$ animals, $P=0.9731$, $t=0.3908$, d.f. = 18) in any genotype. Data normalized to the control, non-deprived cortex within each animal. All data are presented as the mean ± s.e.m.

even in wild-type animals (Fig. 2h,i,l). This is consistent with previous work demonstrating that microglia preferentially engulf presynaptic inputs[2,27]. We further confirmed that this effect was through microglial CX3CR1; CX3CR1 was highly enriched in microglia in control and deprived barrel cortices versus other neural or glial cell types (Supplementary Fig. 5i–l). In addition, while peripheral CD45$^+$ monocytes and F4/80$^+$ macrophages expressed CX3CR1 in the whisker pad, this expression pattern did not change following whisker lesioning (Supplementary Fig. 5c,h). We further measured macrophage recruitment to the whisker follicles following whisker lesioning as well as immunostaining for ATF3 in *Cx3cr1*$^{-/-}$ mice (Supplementary Fig. 5). All these responses were comparable to *Cx3cr1*$^{+/-}$ controls (Supplementary Fig. 2). Last, we assessed TC input elimination following whisker trimming and found that TC input elimination elicited in this paradigm was also CX3CR1-dependent (Supplementary Fig. 5f,g). Together, these results suggest that synapse elimination defects in *Cx3cr1*$^{-/-}$ mice are not secondary to changes in injury, wound healing, or neuronal stress responses, and are most consistent with microglial CX3CR1 mediating synapse elimination in the barrel cortex.

To further determine whether CX3CR1-dependent defects in TC input elimination are long-lasting, we lesioned whiskers at P4 and then assessed structural and functional remodeling at ≥6 weeks of age (Fig. 3). Similar to 6 days post-whisker removal, we observed a significant decrease in structural TC inputs in the deprived adult (P90) *Cx3cr1*$^{+/+}$ barrel cortex (Fig. 3a), which was blocked in *Cx3cr1*$^{-/-}$ mice (Fig. 3b). To assess functional connectivity, we also performed electrophysiological recordings in ≥6 week *Cx3cr1*$^{-/-}$ and *Cx3cr1*$^{+/+}$ mice. We observed a significant decrease in spontaneous excitatory postsynaptic current (sEPSC) frequency and amplitude in layer IV stellate neurons within the deprived cortex in *Cx3cr1*$^{+/+}$ mice (Fig. 3c,d), which was consistent with the decreased number and strength of functional synapses in the deprived cortex. When we assessed the same parameters in *Cx3cr1*$^{-/-}$ littermates (Fig. 3c,e), there was no longer a significant decrease in sEPSC frequency or amplitude in the deprived cortex compared with the control cortex. Interestingly, there was evidence of a decrease in baseline sEPSC frequency and amplitude in *Cx3cr1*$^{-/-}$ mice compared with *Cx3cr1*$^{+/+}$ littermates, suggesting that CX3CR1 signaling might regulate these aspects of functional synapse maturation within the barrel cortex. These data establish that microglial CX3CR1 signaling is critical for long-term remodeling of structural and functional synapses in the barrel cortex several synapses away from a peripheral sensory lesion.

CX3CR1 and CX3CL1 regulate microglia-mediated engulfment of TC synapses. While microglial CX3CR1 signaling has previously been implicated to play an important role in regulating synapse development[13–15], the mechanism by which CX3CR1 exerts these effects is largely unknown. It has been suggested that CX3CR1, a chemokine receptor, is necessary for microglial recruitment to synapses. Similar to previously published work in the barrel cortex[14], we found that microglia in neonatal *Cx3cr1*$^{+/-}$ mice were concentrated in barrel septa and infiltrated the barrel centers at P6 and P7, and this was delayed to P8 in *Cx3cr1*$^{-/-}$ mice (Fig. 4a,b; Supplementary Fig. 6). There was no difference in the total numbers of microglia in the *Cx3cr1*$^{-/-}$ barrel cortices compared with those in *Cx3cr1*$^{+/-}$ mice (Supplementary Fig. 6). We then identified that recruitment and the overall density of microglia were largely unaffected in *Cx3cr1*$^{+/-}$ and *Cx3cr1*$^{-/-}$ littermates following whisker lesioning (Fig. 4a,b; Supplementary Fig. 6). There was still a transient delay in the recruitment of microglia to barrel centers in *Cx3cr1*$^{-/-}$ mice in both control and deprived barrel cortices; however, the numbers of microglia within barrel centers were indistinguishable from *Cx3cr1*$^{+/-}$ mice by P8. Given that the bulk of TC synapse elimination occurs after P8 in the current paradigm (Fig. 1a–c), the delay in recruitment of microglia to the barrel centers in <P8 *Cx3cr1*$^{-/-}$ mice likely does not explain the sustained defect in synapse elimination in *Cx3cr1*$^{-/-}$ mice. To more closely assess microglial–synapse interactions in *Cx3cr1*$^{-/-}$ mice in response to whisker removal, we next analyzed microglia-mediated TC input engulfment. Unlike CR3-KO mice (Supplementary Fig. 4), loss of CX3CR1 blocked TC input engulfment by microglia in the deprived barrel cortex at P5 and P9 (Fig. 4c–h). Together, these data demonstrate that CX3CR1 signaling modulates microglia-mediated synaptic engulfment, and blockade of this engulfment results in sustained defects in structural and functional synapse elimination following a peripheral sensory lesion.

We next sought to understand the signals upstream of CX3CR1 necessary for TC synapse elimination by microglia by assessing mice deficient in fractalkine (CX3CL1), the canonical and only known in vivo ligand of CX3CR1 (ref. [28]). Similar to *Cx3cr1*$^{-/-}$ mice, we observed significant defects in the elimination of TC inputs 6 days post-whisker removal in the *Cx3cl1*$^{-/-}$ barrel cortex (Fig. 5a–f). This synapse-elimination defect was accompanied by a blockade of TC input engulfment by microglia (Fig. 5g–i) in *Cx3cl1*$^{-/-}$ mice, which phenocopies defects in *Cx3cr1*$^{-/-}$ mice. These data identify CX3CL1 as a novel regulator of TC synapse remodeling and microglia-mediated synapse engulfment and strongly suggest that microglia eliminate TC inputs through CX3CR1–CX3CL1 signaling.

***Cx3cl1* is highly enriched in neurons in the barrel cortex but its transcription is not modulated by whisker lesioning.** To further explore the mechanism by which CX3CL1 signals to CX3CR1 to regulate TC synapse elimination, we performed single-cell RNA-seq in the deprived and non-deprived barrel cortices of *Cx3cr1*$^{+/-}$ and *Cx3cr1*$^{-/-}$ mice. *Cx3cr1*$^{+/-}$ mice were used as controls as these were the animals used for initial synaptic remodeling and engulfment analyses (Fig. 1). Twenty-four hours after unilateral whisker lesioning, deprived and control barrel cortices were microdissected from each animal, and single-cell RNA-seq was performed using inDrops[29]. Following principal component analysis (PCA), we identified 27 distinct clusters of CNS cells within the barrel cortex. These results were reproducible across biological replicates, with an average read depth of 8,815 reads per cell. (Fig. 6; Supplementary Figs. 7 and 8). In agreement with a recent single-cell RNA-seq study of the adult visual cortex[30], we observed gene expression changes in neurons and glia following manipulation of sensory experience (Supplementary Figs. 9 and 10). To our knowledge, this is the first analysis of sensory lesion and CX3CR1-dependent gene expression in the developing somatosensory cortex at single-cell resolution. From this dataset, we identified some potentially interesting differences in glial, including microglial, gene expression changes following whisker lesioning, which were CX3CR1-dependent (Supplementary Fig. 10). Notably, compared to neurons, the numbers of glial cells sequenced was relatively low for individual genotypes (Supplementary Fig. 10g). Therefore, future investigations are necessary to validate gene expression changes in glia. For the remainder of the study, we focused our analyses on whisker lesion-induced changes in *Cx3cl1* and related genes.

Similar to previous work[28], we observed enrichment of *Cx3cl1* mRNA in neurons compared to non-neuronal cells (Fig. 6b,c). However, we found no significant difference in *Cx3cl1* mRNA in the deprived compared with control barrel cortex in any cell type (Fig. 6c). These data were confirmed by in situ hybridization (Fig. 6d,e), RNA-seq of whole barrel cortex (Fig. 1e), and quantitative PCR (qPCR) from the barrel cortex and VPM nucleus of the thalamus (Fig. 6f,g; Supplementary Fig. 11). These data demonstrate that CX3CL1 is derived from neurons, but its transcription in the barrel cortex and thalamus is unchanged following peripheral sensory lesioning.

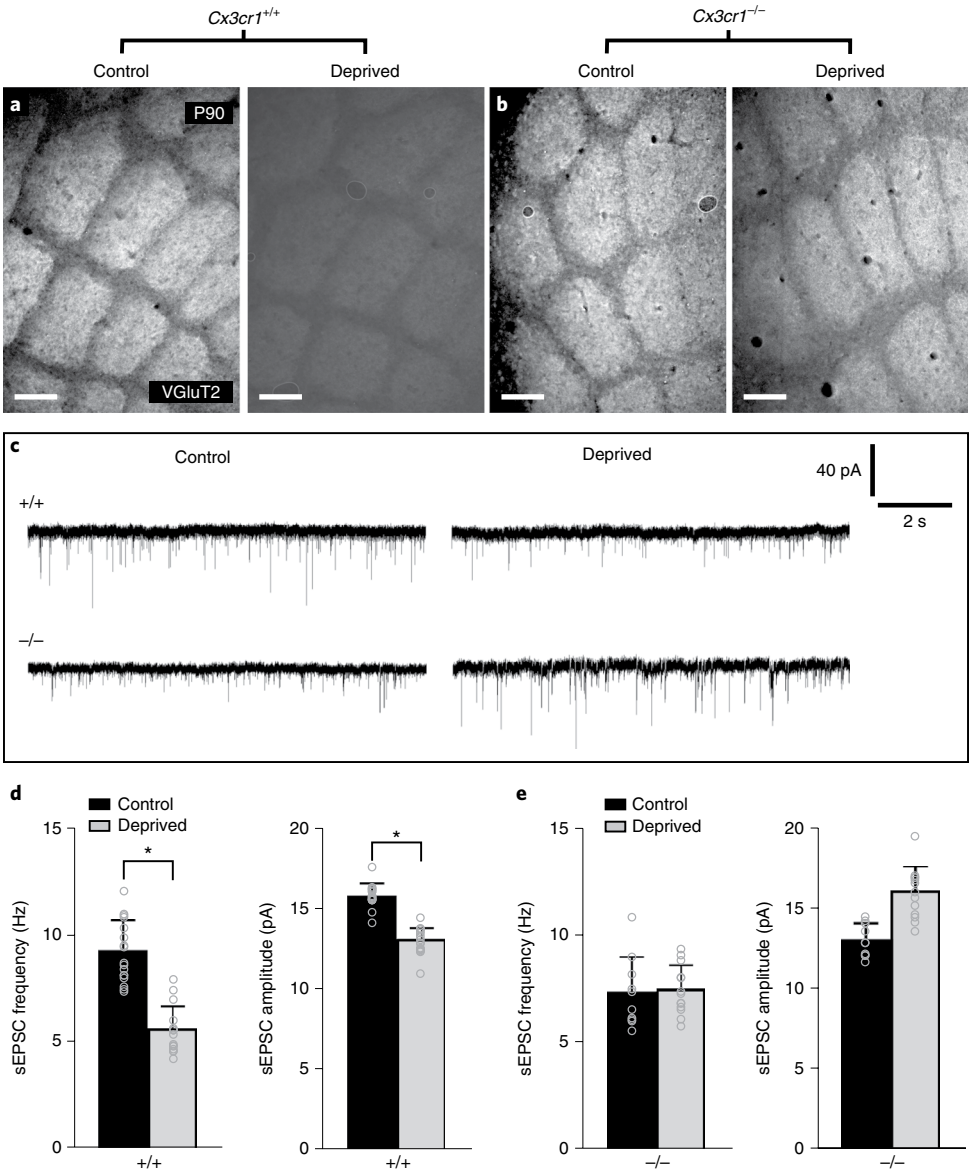

Fig. 3 | CX3CR1 deficiency blocks structural and functional synaptic remodeling long term. a,**b**, VGluT2 immunolabeling of TC inputs in tangential sections of the control and deprived barrel cortex in P90 *Cx3cr1*$^{+/+}$ (**a**) and *Cx3cr1*$^{-/-}$ (**b**) littermates. TC inputs remain in *Cx3cr1*$^{-/-}$ mice after sustained whisker removal (**b**, right). Scale bars, 150 µm. Representative images taken from two independent experiments/animals. **c**, Representative sEPSC traces from layer IV stellate neurons for the control and deprived barrel cortices of P42–P56 *Cx3cr1*$^{+/+}$ and *Cx3cr1*$^{-/-}$ mice. **d**,**e**, Quantification of stellate neuron sEPSC frequency and amplitude in *Cx3cr1*$^{+/+}$ mice (**d**; sEPSC frequency, $n=17$ control and 16 deprived cells from 3 *Cx3cr1*$^{+/+}$ littermates, two-tailed Student's *t*-test, $^{*}P=0.0484$, $t=2.054$, d.f. = 31; sEPSC amplitude, two-tailed Student's *t*-test, $^{*}P=0.0105$, $t=2.723$, d.f. = 31) and *Cx3cr1*$^{-/-}$ mice (**e**; sEPSC frequency, $n=10$ control and 13 deprived cells from 3 *Cx3cr1*$^{-/-}$ littermates, two-tailed Student's *t*-test, $P=0.1286$, $t=1.582$, d.f. = 21; sEPSC amplitude, two-tailed Student's *t*-test, $P=0.9432$, $t=0.07205$, d.f. = 21) in the deprived compared with the contralateral control barrel cortex. *Cx3cr1*$^{-/-}$ mice show no significant decrease in stellate neuron sEPSC frequency or amplitude. All data are presented as the mean ± s.e.m.

***Adam10* is increased in neurons and microglia within the barrel cortex following whisker lesioning.** CX3CL1 can exist in a membrane or a secreted form[28]. The latter is produced following cleavage of the membrane-bound form by metalloproteases[31]. Therefore, we hypothesized that this post-translational processing of CX3CL1, versus its transcription, may be modified following whisker lesioning. Within our single-cell RNA-seq dataset, we identified *Adam10*, a gene encoding a metalloprotease previously shown to be regulated by neuronal activity[32] and known to cleave CX3CL1 (ref. [31]) (Fig. 7a), as specifically increased in *Rorb*$^{+}$ layer IV neurons and microglia compared to other cell types following whisker lesioning (Fig. 7b,c; Supplementary Fig. 9). We validated these single-cell RNA-seq results and demonstrated using in situ hybridization that *Adam10* mRNA was increased in *Rorb*$^{+}$ layer IV neurons in the deprived barrel cortex relative to control (Fig. 7d,e). We then assessed microglial *Adam10* expression by in situ hybridization in the barrel cortex (Fig. 7g–i). Similar to the analysis of *Rorb*$^{+}$ neurons (Fig. 7e), we averaged the data across all the microglia. While this analysis revealed no significant difference in total microglial *Adam10* expression following whisker lesioning (Fig. 7h), we observed a subset of microglia that had high *Adam10* expression in the deprived cortex (Fig. 7g). Therefore, we binned the data on the basis of *Adam10* puncta per cell and found that microglia with the highest expression of *Adam10* (>15 puncta per cell) were significantly increased in the deprived compared with control barrel cortex (Fig. 7i).

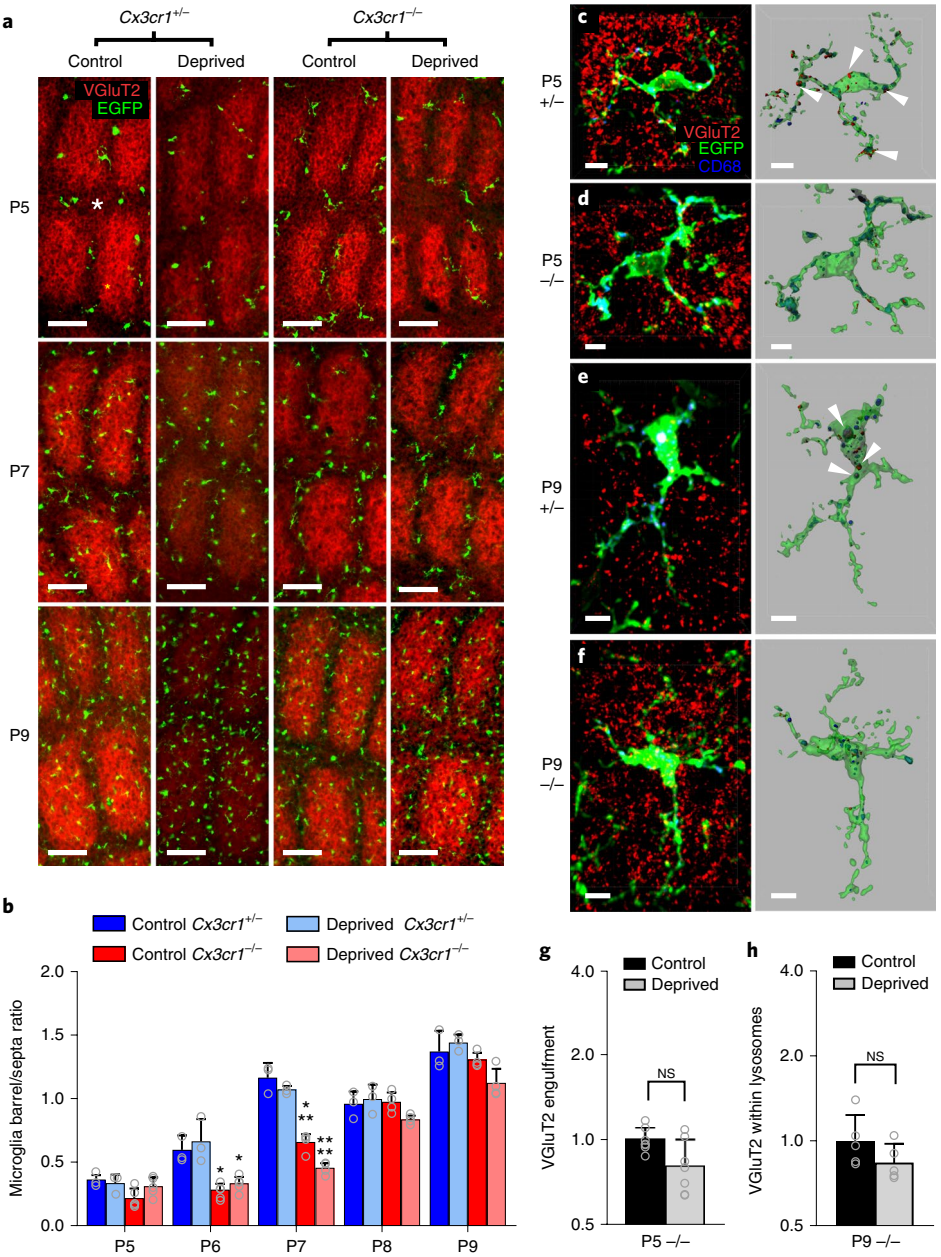

Fig. 4 | Microglial engulfment of TC inputs following whisker lesioning is CX3CR1-dependent. a, Representative images of microglia within the barrel cortex labeled by transgenic expression of EGFP under the control of *Cx3cr1*(green) and TC inputs labeled with anti-VGluT2 (red). **b**, Quantification of the ratio of microglia localized to the septa (denoted by the white asterisk at P5) compared with the barrels (denoted by a yellow asterisk at P5) with or without whisker deprivation. In both deprived and non-deprived barrel cortices, microglia begin to infiltrate the barrel centers from the septa by P6–7 in *Cx3cr1*$^{+/-}$ mice, which is delayed to P8 in *Cx3cr1*$^{-/-}$ mice. There is no significant difference by P8. Two-way ANOVA and Tukey's post hoc test, control *Cx3cr1*$^{+/-}$ versus control *Cx3cr1*$^{-/-}$ at P6, $n=3$ *Cx3cr1*$^{+/-}$ and 5 *Cx3cr1*$^{-/-}$ littermates, $^{*}P=0.0394$, $q=3.887$, d.f. = 54; deprived *Cx3cr1*$^{+/-}$ versus deprived *Cx3cr1*$^{-/-}$ at P6, $n=3$ *Cx3cr1*$^{+/-}$ and 5 *Cx3cr1*$^{-/-}$ littermates, $^{*}P=0.0273$, $q=4.092$, d.f. = 54; *Cx3cr1*$^{+/-}$ versus control *Cx3cr1*$^{-/-}$ at P7, $n=3$ *Cx3cr1*$^{+/-}$ and 4 *Cx3cr1*$^{-/-}$ littermates, $^{***}P=0.0005$, $q=5.996$, d.f. = 54; deprived *Cx3cr1*$^{+/-}$ versus deprived *Cx3cr1*$^{-/-}$ at P7, $n=3$ *Cx3cr1*$^{+/-}$ and 4 *Cx3cr1*$^{-/-}$ littermates, $^{****}P<0.0001$, $q=7.32$, d.f. = 54. **c**–**f**, Representative microglia from the deprived barrel cortex of *Cx3cr1*$^{+/-}$ and *Cx3cr1*$^{-/-}$ mice 24 h and 5 days after whisker lesioning. Left: raw fluorescent image with microglia (EGFP, green), VGluT2 (red), and lysosomes (CD68, blue). Right: 3D-rendered microglia within layer IV of the deprived barrel cortex 24 h (**c** and **d**) and 5 days (**e** and **f**) post deprivation. Arrowheads denote examples of engulfed TC inputs in *Cx3cr1*$^{+/-}$ barrel cortex (**c** and **e**), which are largely absent in *Cx3cr1*$^{-/-}$ mice (**d** and **f**). Scale bars, 5 µm. **g**,**h**, Quantification of engulfment in *Cx3cr1*$^{-/-}$ mice 24 h (**g**; two-tailed Student's *t*-test, $n=8$ littermate animals, $P=0.3668$, $t=0.938$, d.f. = 12) and 5 days (**h**; two-tailed Student's *t*-test, $n=5$ littermate animals, $P=0.5619$, $t=0.6051$, d.f. = 8) post deprivation reveals no significant increase in engulfed TC inputs in the control versus deprived barrel cortex at any time point. Engulfment data normalized to the control, non-deprived hemisphere within each animal. All data are presented as the mean ± s.e.m.

To further validate that the expression of *Adam10* is upregulated, we performed qPCR from whole barrel cortex and observed a similar increase in total *Adam10* mRNA 24 h post-whisker lesioning (Fig. 7f). An analysis of bulk RNA-seq from whole barrel cortex (Fig. 1d–f) showed a similar effect (Fig. 7j,k). These RNA-seq data also revealed increases in molecules known to interact with and

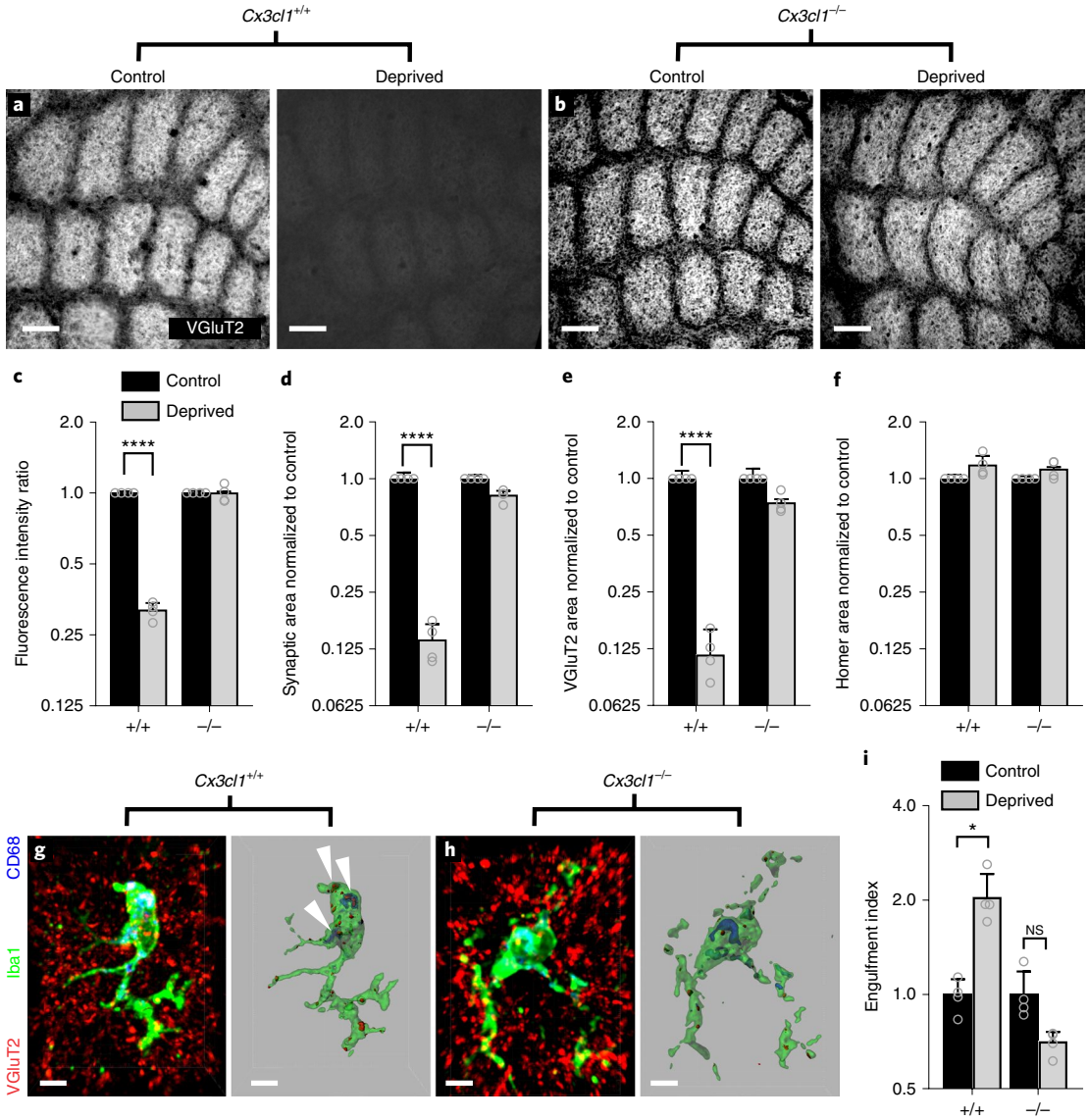

Fig. 5 | CX3CL1 is necessary for TC input engulfment and elimination after sensory lesioning. a,**b**, VGluT2-immunolabeled TC inputs within tangential sections of control and deprived barrel cortices in *Cx3cl1*$^{+/+}$ (**a**) and *Cx3cl1*$^{-/-}$ mice (**b**). Scale bars, 150 µm **c**, Quantification of fluorescence intensity of VGluT2^{+} TC input 6 days after deprivation shows a significant decrease in VGluT2 fluorescence intensity in *Cx3cl1*$^{+/+}$ mice, which is blocked in *Cx3cl1*$^{-/-}$ littermates. Data normalized to the control, non-deprived hemisphere within each animal. Two-way ANOVA with Sidak's post hoc test, $n=4$ animals per genotype, $^{****}P<0.0001$, $t=28.3$, d.f. = 12. **d**–**f**, Quantification of high-magnification images of synaptic components in the barrel centers 6 days after whisker removal reveals a significant decrease in structural synapses (**d**; VGluT2 colocalized with Homer; two-way ANOVA with Sidak's post hoc test, $n=4$ animals per genotype, *Cx3cl1*$^{+/+}$ control versus deprived, $^{****}P<0.0001$, $t=11.66$, d.f. = 12) and VGluT2^{+} presynaptic terminals (**e**; two-way ANOVA with Sidak's post hoc test, $n=4$ animals per genotype, *Cx3cl1*$^{+/+}$ control versus deprived, $^{****}P<0.0001$, $t=7.418$, d.f. = 12) in *Cx3cl1*$^{+/+}$ mice but no significant change in *Cx3cl1*$^{-/-}$ littermates (colocalized area, $P=0.0642$, $t=2.415$, d.f. = 12; VGluT2 area, $P=0.1071$, $t=2.125$, d.f. = 12). There was no significant change in density of Homer immunoreactivity in *Cx3cl1*$^{+/+}$ or *Cx3cl1*$^{-/-}$ mice following whisker deprivation (**f**; two-way ANOVA with Sidak's post hoc test, $n=4$ animals per genotype, no significance). Data normalized to the control, non-deprived hemisphere within each animal. **g**,**h**, Representative microglia from the deprived barrel cortex of *Cx3cl1*$^{+/+}$ (**g**) and *Cx3cl1*$^{-/-}$ (**h**) mice. Left: raw fluorescent image with microglia (anti-Iba1, green) VGluT2 inputs (red) and lysosomes (anti-CD68, blue) labeled. Right: 3D-surface rendering of these cells. Engulfed VGluT2 (red) immunoreactive TC inputs within microglia are visualized in *Cx3cl1*$^{+/+}$ microglia (**g**, arrowheads) but not *Cx3cl1*$^{-/-}$ microglia (**h**). Scale bars, 5 µm. **i**, Quantification of VGluT2 engulfment 24 h after whisker removal reveals that *Cx3cl1*$^{-/-}$ microglia fail to engulf TC inputs following sensory deprivation. Data normalized to engulfment in the control hemisphere within each animal. Two-way ANOVA with Sidak's post hoc test, $n=4$ littermates per genotype, *Cx3cl1*$^{+/+}$ control versus deprived $^{*}P=0.0111$, $t=3.369$, d.f. = 12; *Cx3cl1*$^{-/-}$ control versus deprived $P=0.5963$, $t=0.9422$, d.f. = 12. All data are presented as the mean ± s.e.m.

regulate ADAM10 activity at the membrane (for example, tetraspanins (*Tspn5* and *Tspn14*); Fig. 7k). These data demonstrate that ADAM10, a protease that cleaves CX3CL1 into a secreted form, is induced in layer IV excitatory neurons and a subset of microglia within the barrel cortex following sensory lesioning.

Pharmacological inactivation of ADAM10 phenocopies TC synapse elimination defects in *Cx3cr1*$^{-/-}$ and *Cx3cl1*$^{-/-}$ mice. To determine whether induction of *Adam10* expression in response to whisker lesioning translated to circuit-level changes in TC synapse remodeling as observed in *Cx3cr1*$^{-/-}$ and *Cx3cl1*$^{-/-}$ mice,

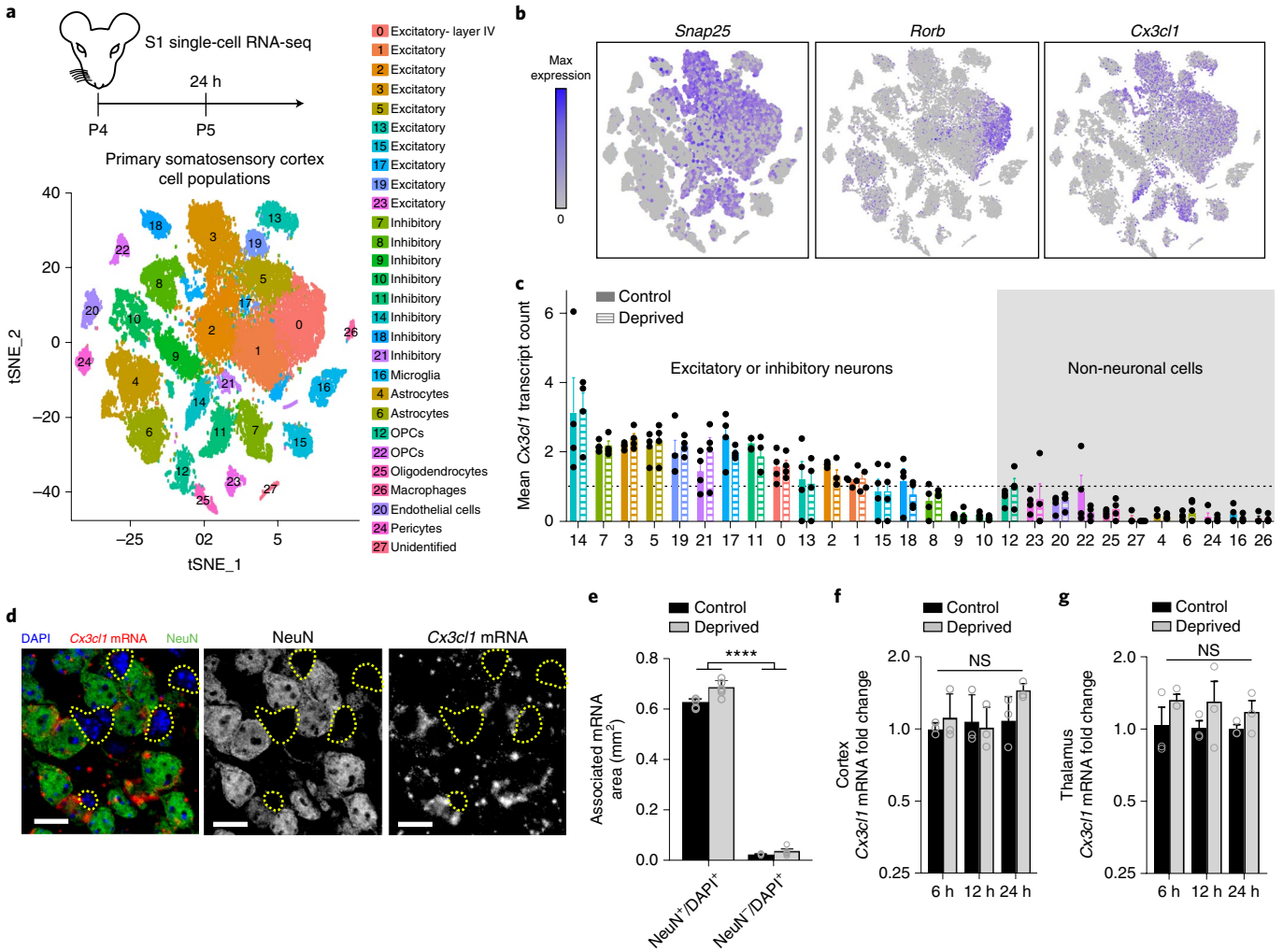

Fig. 6 | *Cx3cl1* is highly enriched in neurons in the barrel cortex but its transcription is not modulated by whisker lesioning. a, Timeline for whisker removal and single-cell RNA-seq analysis. P4 mice ($n=4$ *Cx3cr1*$^{+/-}$, $n=4$ *Cx3cr1*$^{-/-}$) underwent unilateral whisker lesioning. Twenty-four hours later, barrel cortices were prepared for single-cell RNA-seq. A t-distributed stochastic neighbor embedding (t-SNE) plot shows 27 distinct cell populations in the barrel cortex clustered by PCA (Supplementary Fig. 7). OPCs, oligodendrocyte percursor cells. **b**, t-SNE plots for *Snap25* and *Cx3cl1* across all 27 clusters. *Cx3cl1* is enriched in most SNAP25^{+} neuronal clusters. **c**, Mean *Cx3cl1* RNA transcript counts per condition in *Cx3cr1*$^{+/-}$ animals. Colors of the bars and numbers on the *x* axis correspond to those in the key in **a**. Each data point is the mean expression across cells within each individual *Cx3cr1*$^{+/-}$ hemisphere (control or deprived). Data points at or below the broken line indicates 1 transcript or no expression. *Cx3cl1* is enriched in neurons but its expression is unchanged following whisker lesioning across all cell types. **d**, In situ hybridization for *Cx3cl1* (red) and immunohistochemistry for NeuN to label neurons (green) in *Cx3cl1*$^{+/+}$ deprived barrel cortices validates that *Cx3cl1* is enriched in NeuN^{+} neurons compared with non-neuronal cells (NeuN^{-}, yellow broken lines). Scale bars, 15 µm. **e**, Quantification of in situ hybridization for *Cx3cl1* reveals enrichment in neuronal (NeuN^{+} and DAPI^{+}) versus non-neuronal (NeuN^{-} and DAPI^{+}) cells and no change in expression 24 h post-whisker lesioning. Two-way ANOVA with Sidak's post hoc test, control NeuN^{+}/DAPI^{+} versus control NeuN^{-}/DAPI^{+}, $^{****}P<0.0001$, $t=25.78$, d.f. = 20; deprived NeuN^{+}/DAPI^{+} versus deprived NeuN^{-}/DAPI^{+}, $^{****}P<0.0001$, $t=27.7$, d.f. = 27; control NeuN^{+}/DAPI^{+} versus deprived NeuN^{-}/DAPI^{+}, $^{****}P<0.0001$, $t=25.19$, d.f. = 20; deprived NeuN^{+}/DAPI^{+} versus control NeuN^{-}/DAPI^{+}, $^{****}P<0.0001$, $t=28.29$, d.f. = 20; $n=6$ images from 3 animals (3 males). All data are presented as the mean ± s.e.m. **f**,**g**, qPCR for *Cx3cl1* expression in the barrel cortex (**f**) and VPM nucleus of the thalamus (**g**) 6, 12, 24, and 72 h after whisker lesioning in *Cx3cr1*$^{+/+}$ mice in the control and deprived barrel cortices. Two-way ANOVA with Sidak's post hoc test, $n=3$ animals per time point; 6 h barrel cortex control versus deprived, $P=0.9958$, $t=0.3299$, d.f. = 16; 12 h barrel cortex control versus deprived, $P=0.9996$, $t=0.1766$, d.f. = 16; 24 h barrel cortex control versus deprived, $P=0.7804$, $t=1.036$, d.f. = 16; 72 h barrel cortex control versus deprived, $P=0.9722$, $t=0.5476$, d.f. = 16; 6 h thalamus control versus deprived, $P=0.5295$, $t=1.287$, d.f. = 12; 12 h thalamus control versus deprived, $P=0.5041$, $t=1.329$, d.f. = 12; 24 h thalamus control versus deprived, $P=0.8261$, $t=0.7954$, d.f. = 12. All data are presented as the mean ± s.e.m.

we pharmacologically inhibited ADAM10. Whiskers were lesioned at P4 and a pharmacological inhibitor of ADAM10 (GI254023X, 25 mg per kg), which was previously demonstrated in vivo to cross the blood–brain barrier and to specifically inhibit ADAM10 compared with other ADAM family members[33–35], was administered intraperitoneally daily, starting at the time of whisker lesioning (Fig. 8a). TC synapse engulfment and elimination were subsequently assessed in the control and deprived barrel cortices. Identical to *Cx3cr1*$^{-/-}$ and *Cx3cl1*$^{-/-}$ mice, daily administration of the ADAM10 inhibitor (25 mg per kg) by intraperitoneal injection at P4–P10 resulted in significant disruption of TC input elimination following whisker lesioning (Fig. 8b,c) and blockade of microglia-mediated engulfment of TC inputs (Fig. 8d–i). These data suggest a mechanism by which post-translational modification of CX3CL1 by ADAM10 is increased in neurons following sensory lesioning. This secreted CX3CL1 then signals to microglia via CX3CR1 to eliminate synapses.

Discussion

We have identified a novel mechanism by which neurons signal to microglia to remodel synapses in response to sensory loss and dampened neural activity. We showed that whisker removal induces microglial synaptic engulfment and synapse elimination via CX3CR1–CX3CL1, but not CR3, signaling. We further showed by single-cell RNA-seq and other validation methods that *Cx3cl1* is enriched in cortical neurons and that *Adam10*, a gene encoding a metalloprotease known to cleave CX3CL1 into a secreted form, is specifically induced in layer IV excitatory neurons and a subset of microglia following sensory lesioning. This single-cell transcriptomic study of the developing barrel cortex resulted in a rich dataset and is likely a valuable resource for assessing gene expression in glia and neurons. Finally, to further support our single-cell RNA-seq findings, pharmacological inhibition of ADAM10 phenocopied TC synapse elimination defects observed in CX3CR1-deficient mice and CX3CL1-deficient mice. Together, our data suggest a mechanism by which post-translational processing of CX3CL1 in neurons by ADAM10 is regulated by changes in neural activity following a peripheral sensory lesion. Cleaved CX3CL1 can then signal to microglia to initiate engulfment and elimination of synapses via CX3CR1. These data provide a new mechanism by which TC synapses remodel in response to peripheral sensory loss several synapses away.

Previous studies have identified that microglia contact and/or engulf synaptic elements and that these interactions are activity-dependent[1,2,25]. However, the mechanisms underlying these activity-dependent microglia–synapse interactions and the neuron-derived signals driving this process were largely unknown. Another transcriptional profiling study had demonstrated that, under basal conditions, microglia express a number of transcripts for sensing endogenous ligands and microbes, which was termed the 'sensome'[36]. Our data provide a role for one key microglial sensome gene, *Cx3cr1*, in synapse elimination following manipulation of circuit activity via whisker lesioning or trimming. This is consistent with work in a seizure model, whereby CX3CR1 was suggested to modulate microglia–synapse contact in response to activity[37]. CX3CR1 is enriched in microglia versus other CNS-resident neural and glial cell types, and we showed that microglial synaptic engulfment is primarily affected following sensory lesioning in *Cx3cr1*$^{-/-}$ mice. Thus, our results strongly point towards microglial CX3CR1 signaling in regulating engulfment and synapse elimination. Although less likely, it is important to consider the contribution of other tissue-resident CX3CR1-expressing macrophages (for example, skin and perivascular). This would require the development of new mice to specifically ablate CX3CR1 in microglia versus these other macrophage populations.

Our study raises a new question regarding how upstream and downstream CX3CR1 signaling is regulating microglial engulfment and synapse elimination. Upstream of CX3CR1, we identified a new role for neuron-derived CX3CL1 and ADAM10 in microglia-mediated synapse elimination. Going forward, it will be important to elucidate precisely how ADAM10 is modulated in neurons and microglia following sensory lesioning. This includes developing new tools to monitor CX3CL1 cleavage by ADAM10 in specific cells. Downstream of CX3CR1, our single-cell RNA-seq data provide some evidence that there is a downregulation of genes related to phagocytosis in *Cx3cr1*$^{-/-}$ microglia, even without whisker lesioning (Supplementary Fig. 12). This raises the possibility that CX3CR1 signaling could modulate the basal phagocytic state through transcriptional regulation. In addition, our single-cell RNA-seq data revealed that microglia, as well as other glia, modify their gene expression in response to sensory lesioning, which is largely CX3CR1-dependent. While these gene expression changes require further validation, this is an exciting first step in understanding how microglia and other glial cells respond to a changing sensory environment.

One important theme that has emerged from our data is that different neural–immune signaling mechanisms are utilized by microglia to engulf and remodel synaptic connections, and these mechanisms appear to be engaged in a context-dependent manner. CX3CR1 has been identified to regulate synapse maturation in the developing hippocampus and barrel cortex[13,14]. Work in the developing mouse retinogeniculate system has identified major histocompatibility complex (MHC) class I molecules[38,39] and microglial complement-dependent phagocytic signaling[2,4] as key regulators of developmental synaptic pruning. MHC class I molecules[38] and microglial P2RY12 (ref. [26]) regulate ocular dominance plasticity in the visual cortex. Interestingly, retinogeniculate pruning and ocular dominance plasticity occur independent of CX3CR1 (refs. [11,12]). In contrast, we showed that sensory lesion-induced elimination of synapses in the barrel cortex is regulated by CX3CR1–CX3CL1 signaling, but not CR3. While our TC synapse elimination defects

Fig. 7 | ADAM10 is increased in neurons within the barrel cortex following whisker lesioning. a, ADAM10 cleaves CX3CL1 at the membrane (broken line) to produce a secreted form. TM, transmembrane. **b**, t-SNE plot for *Adam10* reveals broad expression across many neuronal and non-neuronal cell types. Single-cell RNA-seq performed on $n=4$ *Cx3cr1*$^{+/-}$ and $n=4$ *Cx3cr1*$^{-/-}$ mice at P5, 24 h after whisker lesioning. **c**, Fold-change of *Adam10* expression by single-cell RNA-seq reveals significant (FDR < 0.10, Monocle2) upregulation specifically in layer IV *Rorb*$^{+}$ neurons and microglia after whisker lesioning. Each data point is the mean fold-change for *Adam10* within each individual *Cx3cr1*$^{+/-}$ deprived hemisphere. Data are presented as the mean ± s.e.m. **d**, In situ hybridization for *Adam10* in the control (left) and deprived (right) barrel cortices. *Adam10* is increased in the majority of *Rorb*$^{+}$ layer IV excitatory neurons (NeuN^{+}, *Rorb*$^{+}$, outlined with yellow dotted line) assessed 24 h post-whisker lesioning compared with neurons in the control barrel cortex. Scale bars, 5 µm. **e**, Quantification of in situ hybridization for *Adam10* puncta colocalized with layer IV neurons. Two-tailed Student's *t*-test, $n=6$ *Cx3cr1*$^{+/+}$ animals, $^{**}P=0.003$, $t=0.3889$, d.f. = 10. Data are presented as the mean ± s.e.m. **f**, qPCR for *Adam10* 24 h post-whisker lesioning in the control and deprived whole barrel cortices reveals a significant increase in *Adam10* 24 h post-whisker lesioning. Two-tailed Student's *t*-test, $n=3$ *Cx3cr1*$^{+/+}$ animals, $^{*}P=0.0241$, $t=3.538$, d.f. = 4. Data presented as the mean ± s.e.m. **g**, In situ hybridization for *Adam10* within *Cx3cr1*$^{EGFP/+}$ microglia (yellow broken lines) in the deprived cortex 24 h post-whisker lesioning reveals increased *Adam10* expression in a subset of microglia after lesioning. Representative images taken in *Cx3cr1*$^{+/+}$ animals across one independent experiment. **h**, Quantification of the average *Adam10* in situ hybridization puncta per microglia averaged across all microglial cells assessed in the barrel cortex shows no significant difference in expression between the control and deprived conditions. Two-tailed Student's *t*-test, $n=3$ *Cx3cr1*$^{+/-}$ animals, $P=0.5547$, $t=0.6439$, d.f. = 4. Data are presented as the mean ± s.e.m. **i**, Further quantification of *Adam10* mRNA puncta within microglia reveals a significant increase in a subset of microglia expressing high levels (≥11 puncta) of *Adam10* in the deprived versus control barrel cortex ($n=36$ deprived microglia, 36 control microglia from 3 *Cx3cr1*$^{+/+}$ animals). One-tailed Chi-square test, $^{*}P=0.0306$, $\chi^2=3.503$, d.f. = 1, $z=1.872$. Data are represented as whole number percentage of the total cell population. **j**, Heatmap with hierarchical clustering distances (scale in top right corner) showing the variation in the expression levels (*z*-scored $\log_2$(RPKM)) of 539 upregulated and 918 downregulated genes following whisker deprivation at P4 identified by bulk RNA-seq from the primary barrel cortex of whisker-lesioned mice (DESeq2 software, $n=5$ mice, P5, related to Fig. 1e). **k**, Line graphs showing *z*-scored $\log_2$(RPKM) changes of *Adam10* and other selected genes encoding known regulators of ADAM10 expression or activity for individual mice. Two-tailed Student's *t*-test; *Adam10*, $^{**}P=0.0060$, $t=5.32$; *Adamts8*, $^{*}P=0.0205$, $t=3.72$; *Itgb3*, $^{*}P=0.0454$, $t=2.87$; *Itgb4*, $^{*}P=0.0106$, $t=4.53$; *Tspan5*, $^{*}P=0.0151$, $t=4.08$; *Tspan14*, $^{***}P=0.0006$, $t=9.80$; $n=5$ animals.

in CX3CR1-deficient mice and CX3CL1-deficient mice are robust, there may be additional pathways that are working with the CX3CR1–CX3CL1 axis that would be worthy of follow-up investigation. One intriguing pathway recently identified to regulate astrocyte–microglia phagocytic crosstalk is interleukin-33 (ref. [40]). In addition, our static imaging results suggest that there may be heterogeneity in the levels of phagocytosis across different microglia, which may be regulated by different immune pathways. While this could be reflected in the nature of static imaging and analyzing fixed time-points, it is an interesting possibility to explore.

Another important point to consider is that differences in immune signaling mechanisms may reflect differences in brain regions, types of synapses, paradigms used for eliciting synaptic changes, or activity patterns. For example, the whisker-lesioning

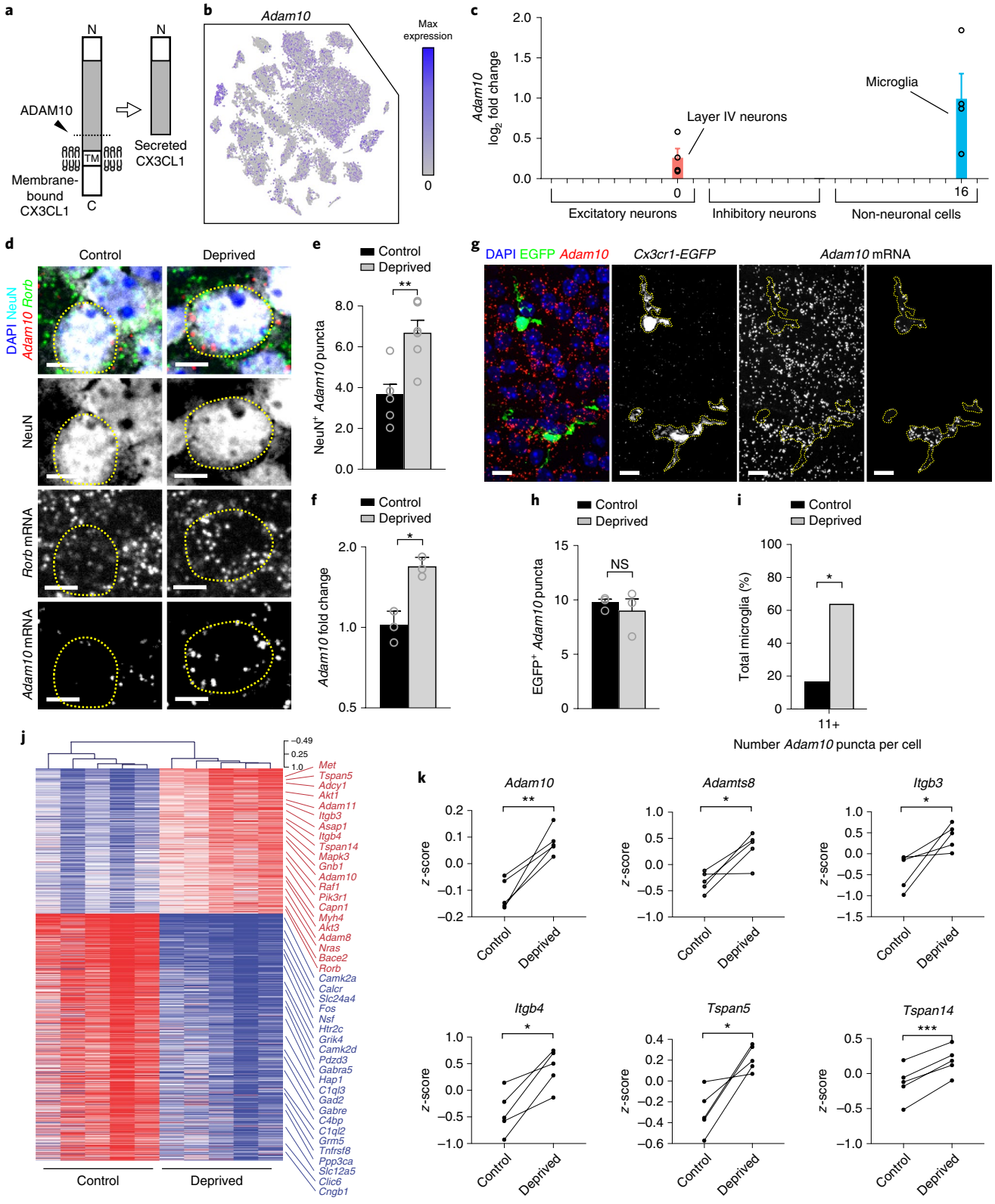

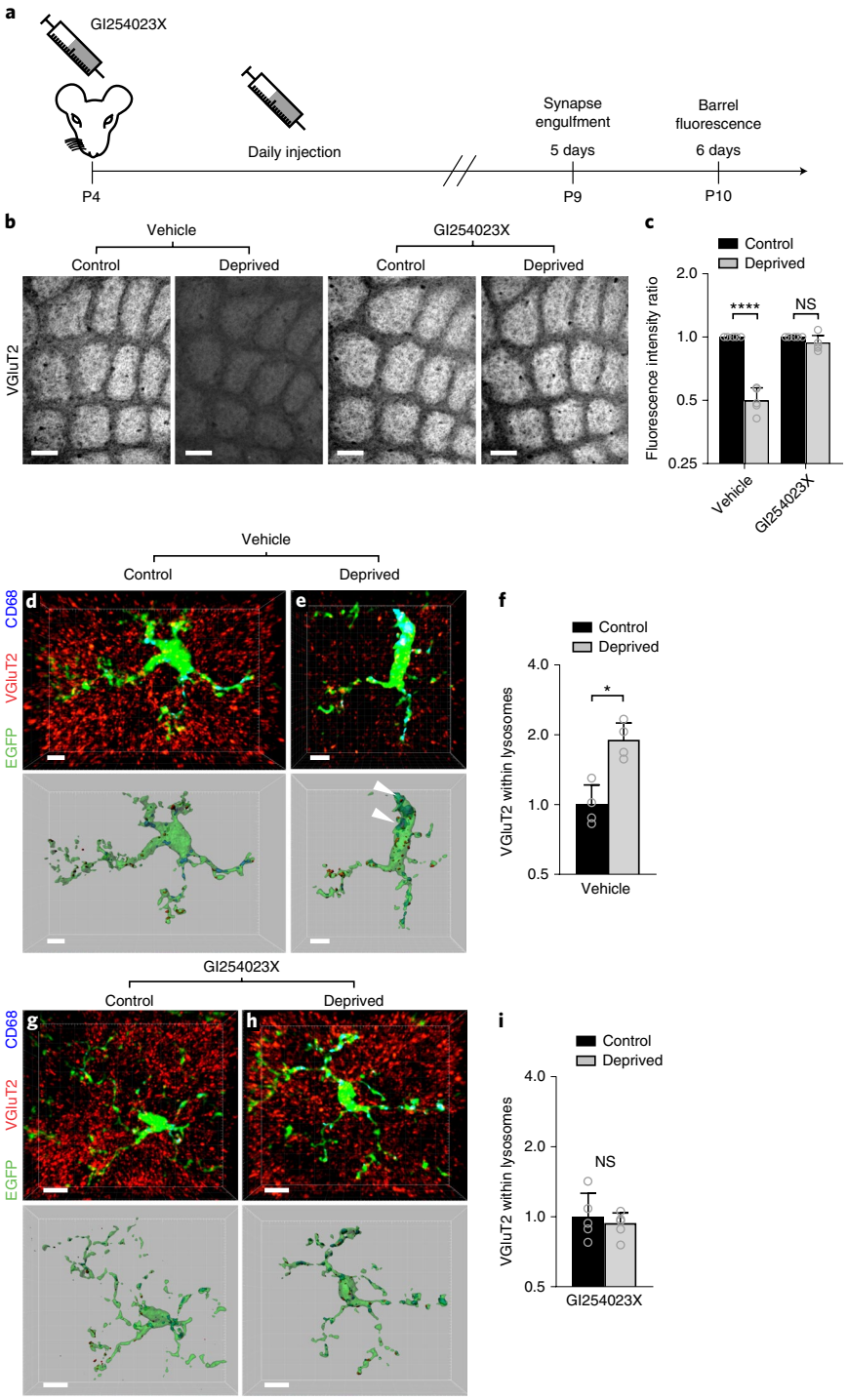

Fig. 8 | Pharmacological inhibition of ADAM10 phenocopies TC synapse elimination defects in *Cx3cr1*$^{-/-}$ and *Cx3cl1*$^{-/-}$ mice. a, Timeline for pharmacological inhibition of ADAM10 via daily intraperitoneal injection of GI254023X (25 mg per kg). **b**, Inhibition of ADAM10 (right), but not vehicle treatment (left), blocks TC input loss, as visualized by immunostaining for VGluT2. Scale bars, 150 µm. **c**, Quantification of VGluT2 immunostaining intensity 5 days post-whisker lesioning and GI254023X injections Two-way ANOVA with Sidak's post hoc test, $n = 5$ *Cx3cr1*$^{+/+}$ animals per condition; vehicle control versus deprived, $^{****}P < 0.0001$, $t = 6.782$, d.f. = 16; GI254023X control versus deprived, $P = 0.9715$, $t = 0.7789$, d.f. = 16. **d**,**e**, Representative microglia from the control (**d**) and deprived (**e**) cortices of vehicle-treated *Cx3cr1*$^{EGFP/+}$ mice. Top: raw fluorescent images with microglia (EGFP, green), VGluT2 inputs (red) and lysosomes (anti-CD68, blue) labeled. Bottom: 3D-surface rendering of these cells. Engulfed VGluT2 (red) immunoreactive TC inputs within microglia are visualized in *Cx3cr1*$^{EGFP/+}$ microglia (**e**, arrowheads) in the deprived cortex but not the control cortex (**d**). Scale bars, 5 µm. **f**, Quantification of engulfed VGluT2 5 days after whisker lesioning reveals increased engulfment in the deprived cortex of vehicle-treated mice. Data normalized to engulfment in the control hemisphere within each animal. One-tailed Student's *t*-test, $n = 4$ *Cx3cr1*$^{EGFP/+}$ mice; control versus deprived $^{*}P = 0.0455$, $t = 2.012$, d.f. = 6. **g**,**h**, Representative microglia from the control (**g**) and deprived (**h**) cortex of GI254023X-treated *Cx3cr1*$^{EGFP/+}$ mice 5 days after whisker lesioning. Scale bars, 5 µm. **i**, Quantification of engulfment 5 days post-whisker lesioning in GI254023X-treated mice reveals a blockade of engulfment following ADAM10 inhibition. Data normalized to engulfment in the control hemisphere within each animal. Two-tailed Student's *t*-test, $n = 4$ *Cx3cr1*$^{EGFP/+}$ mice; control versus deprived $P = 0.8291$, $t = 0.2231$, d.f. = 6. All data are presented as the mean ± s.e.m.

paradigm used here induces injury to the peripheral sensory endings in the snout several synapses away from the barrel cortex. Therefore, this may be an injury versus purely an activity-dependent response. However, there are several lines of evidence arguing against this being an injury response. First, there is no change in neuronal cell death or degeneration following whisker lesioning at P4. Second, there is a similar, albeit delayed, CX3CR1-dependent synapse elimination following whisker trimming. Last, our RNA-seq data demonstrate that there is a downregulation in genes related to neural activity. These data are most consistent with cortical activity modulating CX3CR1–CX3CL1 signaling via ADAM10 and microglia-mediated synapse elimination.

A broad range of neurological disorders—from autism and schizophrenia to traumatic injuries causing loss of eye sight, cutaneous sensation, olfaction, or hearing—all result in changes in sensory inputs and TC connectivity[41–43]. Furthermore, defects in CX3CR1–CX3CL1 signaling and ADAM10 have been identified to either enhance or suppress neurodegeneration in a variety of neurological disease models depending on the disease, insult, and brain region[44–46]. This includes a recent genome-wide association meta-analysis demonstrating that *ADAM10* is an important late-onset Alzheimer's disease loci[47]. Here, we identified that neuronal and microglial ADAM10 is modulated in the cortex by sensory lesioning, and disruption of ADAM10, CX3CL1 (an ADAM10 substrate), or CX3CR1 resulted in profound defects in microglial synaptic engulfment and synapse elimination. This mechanism is particularly intriguing in light of recent data in mouse models of Alzheimer's disease, whereby changes in neural activity modulates microglial morphology, amyloid-β, and amyloid plaques[48,49]. Together, our findings have strong implications for advancing our understanding of how neural activity drives circuit remodeling via microglia and CX3CR1–CX3CL1–ADAM10 signaling. These insights are important for our basic understanding of how neurons communicate with microglia to modulate neural circuits and have substantial translational potential for a variety of neurological disorders.

Online content

Any methods, additional references, Nature Research reporting summaries, source data, statements of code and data availability and associated accession codes are available at https://doi.org/10.1038/s41593-019-0419-y.

Received: 22 June 2018; Accepted: 2 May 2019;
Published online: 17 June 2019

References

1. Wu, Y., Dissing-Olesen, L., MacVicar, B. A. & Stevens, B. Microglia: dynamic mediators of synapse development and plasticity. *Trends Immunol.* **36**, 605–613 (2015).
2. Schafer, D. P. et al. Microglia sculpt postnatal neural circuits in an activity and complement-dependent manner. *Neuron* **74**, 691–705 (2012).
3. Hong, S., Dissing-Olesen, L. & Stevens, B. New insights on the role of microglia in synaptic pruning in health and disease. *Curr. Opin. Neurobiol.* **36**, 128–134 (2016).
4. Stevens, B. et al. The classical complement cascade mediates CNS synapse elimination. *Cell* **131**, 1164–1178 (2007).
5. Vasek, M. J. et al. A complement–microglial axis drives synapse loss during virus-induced memory impairment. *Nature* **534**, 538–543 (2016).
6. Lui, H. et al. Progranulin deficiency promotes circuit-specific synaptic pruning by microglia via complement activation. *Cell* **165**, 921–935 (2016).
7. Hong, S. et al. Complement and microglia mediate early synapse loss in Alzheimer mouse models. *Science* **352**, 712–716 (2016).
8. Wolf, Y., Yona, S., Kim, K. W. & Jung, S. Microglia, seen from the CX3CR1 angle. *Front. Cell. Neurosci.* **7**, 26 (2013).
9. Jung, S. et al. Analysis of fractalkine receptor CX3CR1 function by targeted deletion and *green fluorescent protein* reporter gene insertion. *Mol. Cell. Biol.* **20**, 4106–4114 (2000).
10. Nishiyori, A. et al. Localization of *fractalkine* and *CXCR1* mRNAs in rat brain: does fractalkine play a role in signaling from neuron to microglia? *FEBS Lett.* **429**, 167–172 (1998).
11. Schecter, R. W. et al. Experience-dependent synaptic plasticity in V1 occurs without microglial CX3CR1. *J. Neurosci.* **37**, 10541–10553 (2017).
12. Lowery, R. L., Tremblay, M. E., Hopkins, B. E. & Majewska, A. K. The microglial fractalkine receptor is not required for activity-dependent plasticity in the mouse visual system. *Glia* **65**, 1744–1761 (2017).
13. Paolicelli, R. C. et al. Synaptic pruning by microglia is necessary for normal brain development. *Science* **333**, 1456–1458 (2011).
14. Hoshiko, M., Arnoux, I., Avignone, E., Yamamoto, N. & Audinat, E. Deficiency of the microglial receptor CX3CR1 impairs postnatal functional development of thalamocortical synapses in the barrel cortex. *J. Neurosci.* **32**, 15106–15111 (2012).
15. Zhan, Y. et al. Deficient neuron–microglia signaling results in impaired functional brain connectivity and social behavior. *Nat. Neurosci.* **17**, 400–406 (2014).
16. Woolsey, T. A. & Van der Loos, H. The structural organization of layer IV in the somatosensory region (SI) of mouse cerebral cortex. The description of a cortical field composed of discrete cytoarchitectonic units. *Brain Res.* **17**, 205–242 (1970).
17. Van der Loos, H. & Woolsey, T. A. Somatosensory cortex: structural alterations following early injury to sense organs. *Science* **179**, 395–398 (1973).
18. Fox, K. A critical period for experience-dependent synaptic plasticity in rat barrel cortex. *J. Neurosci.* **12**, 1826–1838 (1992).
19. Glazewski, S., McKenna, M., Jacquin, M. & Fox, K. Experience-dependent depression of vibrissae responses in adolescent rat barrel cortex. *Eur. J. Neurosci.* **10**, 2107–2116 (1998).
20. Oberlaender, M., Ramirez, A. & Bruno, R. M. Sensory experience restructures thalamocortical axons during adulthood. *Neuron* **74**, 648–655 (2012).
21. Wimmer, V. C., Broser, P. J., Kuner, T. & Bruno, R. M. Experience-induced plasticity of thalamocortical axons in both juveniles and adults. *J. Comp. Neurol.* **518**, 4629–4648 (2010).
22. Erzurumlu, R. S. & Kind, P. C. Neural activity: sculptor of 'barrels' in the neocortex. *Trends Neurosci.* **24**, 589–595 (2001).
23. Sadaka, Y., Weinfeld, E., Lev, D. L. & White, E. L. Changes in mouse barrel synapses consequent to sensory deprivation from birth. *J. Comp. Neurol.* **457**, 75–86 (2003).
24. Erzurumlu, R. S. & Gaspar, P. Development and critical period plasticity of the barrel cortex. *Eur. J. Neurosci.* **35**, 1540–1553 (2012).
25. Tremblay, M. E., Lowery, R. L. & Majewska, A. K. Microglial interactions with synapses are modulated by visual experience. *PLoS Biol.* **8**, e1000527 (2010).
26. Sipe, G. O. et al. Microglial P2Y12 is necessary for synaptic plasticity in mouse visual cortex. *Nat. Commun.* **7**, 10905 (2016).
27. Weinhard, L. et al. Microglia remodel synapses by presynaptic trogocytosis and spine head filopodia induction. *Nat. Commun.* **9**, 1228 (2018).
28. Kim, K. W. et al. In vivo structure/function and expression analysis of the CX3C chemokine fractalkine. *Blood* **118**, e156–e167 (2011).
29. Klein, A. M. et al. Droplet barcoding for single-cell transcriptomics applied to embryonic stem cells. *Cell* **161**, 1187–1201 (2015).
30. Hrvatin, S. et al. Single-cell analysis of experience-dependent transcriptomic states in the mouse visual cortex. *Nat. Neurosci.* **21**, 120–129 (2018).
31. Hundhausen, C. et al. The disintegrin-like metalloproteinase ADAM10 is involved in constitutive cleavage of CX3CL1 (fractalkine) and regulates CX3CL1-mediated cell–cell adhesion. *Blood* **102**, 1186–1195 (2003).
32. Suzuki, K. et al. Activity-dependent proteolytic cleavage of neuroligin-1. *Neuron* **76**, 410–422 (2012).
33. Madoux, F. et al. Discovery of an enzyme and substrate selective inhibitor of ADAM10 using an exosite-binding glycosylated substrate. *Sci. Rep.* **6**, 11 (2016).
34. Shackleton, B., Crawford, F. & Bachmeier, C. Inhibition of ADAM10 promotes the clearance of Aβ across the BBB by reducing LRP1 ectodomain shedding. *Fluids Barriers CNS* **13**, 14 (2016).
35. Venkatesh, H. S. et al. Targeting neuronal activity-regulated neuroligin-3 dependency in high-grade glioma. *Nature* **549**, 533–537 (2017).
36. Hickman, S. E. et al. The microglial sensome revealed by direct RNA sequencing. *Nat. Neurosci.* **16**, 1896–1905 (2013).
37. Eyo, U. B. et al. Regulation of physical microglia–neuron interactions by fractalkine signaling after status epilepticus. *eNeuro* **3**, ENEURO.0209-16.2016 (2017).
38. Datwani, A. et al. Classical MHCI molecules regulate retinogeniculate refinement and limit ocular dominance plasticity. *Neuron* **64**, 463–470 (2009).
39. Huh, G. S. et al. Functional requirement for class I MHC in CNS development and plasticity. *Science* **290**, 2155–2159 (2000).
40. Vainchtein, I. D. et al. Astrocyte-derived interleukin-33 promotes microglial synapse engulfment and neural circuit development. *Science* **359**, 1269–1273 (2018).
41. Woodward, N. D., Giraldo-Chica, M., Rogers, B. & Cascio, C. J. Thalamocortical dysconnectivity in autism spectrum disorder: an analysis of the Autism Brain Imaging Data Exchange. *Biol. Psychiatry Cogn. Neurosci. Neuroimaging* **2**, 76–84 (2017).

42. Woodward, N. D., Karbasforoushan, H. & Heckers, S. Thalamocortical dysconnectivity in schizophrenia. *Am. J. Psychiatry* **169**, 1092–1099 (2012).
43. Chen, R., Cohen, L. G. & Hallett, M. Nervous system reorganization following injury. *Neuroscience* **111**, 761–773 (2002).
44. Lauro, C., Catalano, M., Trettel, F. & Limatola, C. Fractalkine in the nervous system: neuroprotective or neurotoxic molecule? *Ann. NY Acad. Sci.* **1351**, 141–148 (2015).
45. Pruessmeyer, J. & Ludwig, A. The good, the bad and the ugly substrates for ADAM10 and ADAM17 in brain pathology, inflammation and cancer. *Semin. Cell Dev. Biol.* **20**, 164–174 (2009).
46. Ransohoff, R. M. & Benveniste, E. N. *Cytokines and the CNS* 2nd edn (Taylor and Francis, 2006).
47. Kunkle, B. W. et al. Genetic meta-analysis of diagnosed Alzheimer's disease identifies new risk loci and implicates Aβ, tau, immunity and lipid processing. *Nat. Genet.* **51**, 414–430 (2019).
48. Iaccarino, H. F. et al. Gamma frequency entrainment attenuates amyloid load and modifies microglia. *Nature* **540**, 230–235 (2016).
49. Martorell, A. J. et al. Multi-sensory gamma stimulation ameliorates Alzheimer's-associated pathology and improves cognition. *Cell* **177**, 256–271. e222 (2019).

Acknowledgements

The authors thank M. Freeman (OHSU), V. Budnik (UMMS), E. Baehrecke (UMMS), M. Francis (UMMS), P. Greer (UMMS), and R. Bruno (Columbia University) for their critical reading of the manuscript. They also thank the following individuals: M. Ansorage (Columbia University) and S. Nelson (Brandeis University) for providing the SERT-Cre mice; Cahill (UMMS) and A. Lotun (UMMS) for assistance with assessing microglia within the barrel cortex; S. Becker (UMMS) and J. Jung (UMMS) for assistance with tissue preparation and whisker-trimming experiments; H. Learnard (UMMS), A. Song (UMMS), Z. Zhang (Boston Children's Hospital), and C. Woolf (Boston Children's Hospital) for assistance with experiments to assess ATF3; and D. Bergles (John's Hopkins) for advice and discussions related to identification of oligodendrocye precursor cells by *Matn4* expression in the single-cell RNA-seq dataset. This work was funded by NIMH-R00MH102351 (D.P.S.), NIMH-R01MH113743 (D.P.S.), NIMH-R21MH115353 (D.P.S. and A.S.), NIH-T32A1095212 (E.M.), the Charles H. Hood Foundation (D.P.S.), the Brain & Behavior Research Foundation (D.P.S.), the Worcester Foundation (D.P.S.), and the Dr. Miriam and Sheldon G. Adelson Medical Research Foundation (D.P.S.).

Author contributions

G.G. and D.P.S. designed the study, performed most experiments, analyzed most data, and wrote the manuscript. K.M.J. assisted in the design of initial experiments, and performed experiments to identify initial synapse remodeling and engulfment phenotypes. L.C., M.A.N., and M.E.G. performed the single-cell sequencing experiments. E.M. performed the in situ hybridization experiments. P.A., A.B., and A.S. performed the bulk RNA-seq experiments of whole barrel cortices. L.L. and A.R.T. performed the electrophysiology experiments. K.-W.K., S.M.B., and B.T.L. performed experiments related to *Cx3cl1*$^{-/-}$ mice, and S.A.L. provided the *Cx3cl1*$^{-/-}$ mice. R.M.R. provided critical input into the study design and feedback on the writing of the manuscript.

Competing interests

The authors declare no competing interests.

Additional information

Supplementary information is available for this paper at https://doi.org/10.1038/s41593-019-0419-y.

Reprints and permissions information is available at www.nature.com/reprints.

Correspondence and requests for materials should be addressed to D.P.S.

Journal peer review information: *Nature Neuroscience* thanks Marie-Ève Tremblay and the other, anonymous, reviewer(s) for their contribution to the peer review of this work.

Publisher's note: Springer Nature remains neutral with regard to jurisdictional claims in published maps and institutional affiliations.

Methods

Animals. SERT-Cre mice were a gift from M. Ansorage (Columbia University) and provided by S. Nelson (Brandeis University). Rosa26-TdTomato mice (Ai14; stock no. 007914), *Cx3cr1*$^{-/-}$ mice (*Cx3cr1*$^{EGFP/EGFP}$; stock no. 005582), CR3-KO mice (stock no. 003991), and C57BL6/J (stock no. 000664) mice were obtained from Jackson Laboratories. Heterozygous breeder pairs were set up for all experiments, and wild-type and heterozygote littermates were used as controls, which included males and females for each genotype. All experiments were performed in accordance with the animal care and use committees and under NIH guidelines for proper animal welfare.

Whisker removal. For sensory lesioning, whiskers were unilaterally removed at P4 with a high-temperature handheld cautery kit (Bovie Medical Corporation) applied to the right whisker pad of anesthetized pups. After whisker removal, pups were placed on a heating pad before animals were returned to their home cage. All animals within one experimental litter were cauterized at the same time blinded to animal genotype. For long-term whisker deprivation, whiskers were removed at P4 and assessed weekly for whisker re-growth. For whisker-trimming experiments, whiskers were unilaterally trimmed using fine surgical scissors (no. 15003-08, Fine Science Tools) from the right whisker pad starting at P4. Whiskers were trimmed twice daily to minimize whisker growth up to P21.

Immunohistochemistry. Animals were perfused with 4% paraformaldehyde (PFA) in 0.1 M phosphate buffer (PB) before brain removal. To visualize the entire barrel field in one plane, the midbrain was dissected from each brain hemisphere and the cortex was then flattened between two slides in 4% PFA overnight. Sections were placed in 30% sucrose in 0.1 M PB for 24 h before 50-µm (for P5–P11 animals) and 40 µm (fro >P40 animals) tangential sections were prepared. Sections were blocked in 10% goat serum, 0.01% Triton X-100 in 0.1 M PB for 1 h before primary immunostaining antibodies were applied overnight. For analysis of synaptic engulfment within microglia, anti-CD68 (1:1,000; cat. no. MCA1957, lot no. 1708, AbD Serotec)[2] and anti-VGluT2 (1:2,000; cat. no. AB2251, lot no. 3101508. MilliporeSigma)[14] were used. Microglia were labeled using either transgenic expression of EGFP (*Cxcr1*$^{EGFP/+}$) or immunostaining for anti-Iba-1 (1:1,000; cat. no. 019-18741, lot no. PTR2404, Wako Chemicals)[2]. For analysis of synapse density, anti-VGluT2 (1:2,000; cat. no. AB2251, lot no. 3101508, MilliporeSigma)[14] and anti-Homer1 (1:1,000; cat. no. 160003, lot no. 1–47, Synaptic Systems)[7,50] were used. For markers of neurodegeneration, cell death, and cell stress, anti-APP (1:1,000; cat. no. 51–2700, lot no. SA243371, Thermo Fisher Scientific)[51], anti-cleaved caspase 3 (1:200; cat. no. 9661, lot no. 45, Cell Signaling Technology)[52], and anti-ATF3 (1:500; cat no. HPA001562, lot no. B116285, Sigma-Aldrich)[53] were used. Anti-NeuN (1:1,000; cat no. ABN91, lot no. 170621, MilliporeSigma)[54] was used as a marker for neuronal cell bodies. Peripheral monocytes/macrophages were labeled with anti-CD45 (Bio-Rad) and anti-F4/80 (1:1,000; cat no. MA-91124, lot no. SJ2459832O, Thermo Fisher Scientific)[55]. For validating the specificity of *Cxcr1-EGFP* expression before and after whisker lesioning, markers for NG2 cells (anti-NG2; 1:200; cat. no. AB5320, lot no. 3061186, MilliporeSigma)[56], astrocytes (anti-ALDH1L1 clone N103/39; 1:1,000; cat. no. MABN495, lot no. 2943620, MilliporeSigma)[57], microglia (anti-P2RY12; 1:100; cat. no. 848002, lot no. B244070, BioLegend)[58], and neurons (anti-NeuN; 1:1,000; cat. no. ABN91, lot no. 170621, MilliporeSigma)[54] were used. Anti-ALDH1L1 clone N103/39 required a 20-min incubation step with L.A.B antigen retrieval solution (Polysciences) before blocking with 10% goat serum, 0.01% Triton X-100 in 0.1 M PB for 1 h.

Fluorescence intensity analysis. For fluorescence intensity analysis, single-plane ×10 epifluorescence images were collected at the same exposure time with a Zeiss Observer microscope equipped with the image acquisition software Zen Blue (Zeiss). One field of view containing all the barrels was collected per hemisphere per animal. The fluorescence intensity within each barrel was quantified similar to what has been previously described[21]. Briefly, each image was analyzed in ImageJ (NIH) whereby all image pixel intensity thresholds were initially set to the full range of 16-bit images before quantification to ensure a consistent pixel range across all images. To sample fluorescence intensity, a circular region of interest (ROI) 75 µm in circumference (4,470.05 µm^2 area) was placed within the center of 15–20 barrels per ×10 field of view. A background ROI outside the barrel field was also taken for each image. The raw integrated density of pixels within each ROI was measured, and each barrel intensity value was background-corrected by subtraction of the background ROI pixel intensity. The average intensity over all barrel ROIs was quantified for each image and then normalized to the control hemisphere within each animal. All data analyses were performed blinded to the genotype.

Engulfment analysis. Engulfment analysis was performed according to previously described methods[2,59]. Briefly, immunostained sections were imaged on a Zeiss Observer Spinning Disk confocal microscope equipped with diode lasers (405 nm, 488 nm, 594 nm, and 647 nm) and the image acquisition software Zen (Zeiss). For each hemisphere, three to five ×63 fields of view within the barrel field were acquired with 50–70 *z*-stack steps at 0.27-µm spacing. Images were first processed in ImageJ (NIH), and then individual images of 15–20 single cells per hemisphere per animal were processed in Imaris (Bitplane) as previously described[2,59]. All image files were blinded for unbiased quantification. All data were then normalized to the control, spared (non-deprived) hemisphere within each animal. Note that *Cx3cr1*$^{+/-}$ littermates were used for comparison to *Cx3cr1*$^{-/-}$ mice, as microglia within both sets of mice are labeled with EGFP and showed similar changes in TC synapses (Fig. 2).

Synapse density analysis. Synapse density analysis was performed blinded to the condition and genotype as previously described[2,7]. Briefly, immunostained sections were imaged on a Zeiss LSM700 scanning confocal microscope equipped with 405 nm, 488 nm, 555 nm, and 639 nm lasers and the software Zen (Zeiss). Synapse density analysis was performed on single-plane confocal images in ImageJ (NIH). Three ×63 fields of view per hemisphere per animal were analyzed. Sample images for each genotype and condition were manually thresholded by eye, and a consistent threshold range was determined (IsoData segmentation method, 85–255). Each channel was thresholded and the function Analyze Particles (ImageJ plugin, NIH) with set parameters for each marker (VGluT2 = 0.2 to infinity; Homer1 = 0.1 to infinity) was used to measure the total pre- and postsynaptic puncta area. To quantify the total synaptic area, Image Calculator (ImageJ plugin, NIH) was used to visualize colocalized pre- and postsynaptic puncta, and then Analyze Particles was used to calculate the total area of colocalized puncta. Data for each hemisphere were averaged across all three fields of view and then normalized to the control hemisphere within each animal.

Bulk RNA-seq. Mice were killed by CO_2 asphyxiation at indicated ages, and brain regions of interest were dissected. Brain tissue from one mouse was immediately homogenized with a motor-driven Teflon glass homogenizer in ice-cold polysome extraction buffer (10 mM HEPES buffer (pH 7.3), 150 mM KCl, 5 mM $MgCl_2$, 0.5 mM dithiothreitol (Sigma) 100 µg ml^{-1} cycloheximide (Sigma), EDTA-free protease inhibitor cocktail (Roche), 10 µl ml^{-1} RNasin (Promega), and Superasin (Applied Biosystems)). Homogenates were centrifuged for 10 min at 2,000 × *g*, 4 °C, to pellet large-cell debris. NP-40 (EMD Biosciences) and 1,2-diheptanoyl-*sn*-glycero-3-phosphocholine (Avanti Polar Lipids) were added to the supernatant at final concentrations of 1% and 30 mM, respectively. After incubation on ice for 5 min, the lysate was centrifuged for 10 min at 13,000 × *g* to pellet insoluble material. RNA was purified from the lysate using a RNeasy Mini kit (Qiagen) following the manufacturer's instructions. RNA integrity was assayed using an RNA Pico chip on a Bioanalyzer 2100 (Agilent), and only samples with RNA integrity numbers >9 were considered for subsequent analysis. Double-stranded complementary DNA was generated from 1–5 ng of RNA using a Nugen Ovation V2 kit (NuGEN) following the manufacturer's instructions. Fragments of 200 bp were obtained by sonicating 500 ng of cDNA per sample using a Covaris-S2 system (duty cycle of 10%; intensity of 5.0; bursts per s of 200; duration of 120 s; mode set to frequency sweeping; power set to 23 W; temperature at 5.5–6 °C). Subsequently, these fragments were used to produce libraries for sequencing using a TruSeq DNA Sample kit (Illumina) following the manufacturer's instructions. The quality of the libraries was assessed using a 2200 TapeStation (Agilent). Multiplexed libraries were directly loaded on a NextSeq 500 (Illumina) with high-output single-read sequencing for 75 cycles. Raw sequencing data were processed using Illumina bcl2fastq2 Conversion Software v.2.17. Raw sequencing reads were mapped to the mouse genome (mm9) using the package TopHat2 (v.2.1.0). Reads were counted using HTSeq-count (v.0.6.0) against the Ensembl v.67 annotation. The read alignment, read count, and quality assessment using metrics such as total mapping rate and mitochondrial and ribosomal mapping rates were done in parallel using an in-house workflow pipeline called SPEctRA. The raw counts were processed through a variance stabilizing transformation (VST) procedure using the package DESeq2 to obtain transformed values that are more suitable than the raw read counts for certain data-mining tasks. PCA was performed on the top 500 most-variable genes across all samples based on the VST data to visually assess whether there were any outliers. Additionally, hierarchical clustering was used to assess the outliers once again to protect against false positives or negatives from the PCA, and the outliers were further justified by the aforementioned quality control metrics as well as experimental metadata. After removal of outliers, all pairwise comparisons were performed on the count data of entire gene transcripts using DESeq2 (v.1.6.3). A cut-off of adjusted P value < 0.05 and mean expression >3.5 were applied. MA plots (representing log-ratio (M) on the y axis and mean average (A) on the x axis) were made using R (v.3.1.1; https://www.R-project.org). For the heatmap, the expression of each gene in $\log_2$ reads per kilobase of transcript per million mapped reads (RPKM) was normalized to the mean across all samples (z-scored). A heatmap with hierarchical clustering was made using Multiple Experiment Viewer 4.8 (v.10.2; http://www.tm4.org/) with Pearson correlation assessed by average link clustering. Bar graphs representing the RPKM of genes and line plots representing z-scored $\log_2$(RPKM) values were made using GraphPad Prism v.5.01 (https://www.graphpad.com).

Single-cell transcriptomics experimental design. Non-deprived, control and deprived barrel cortices from a total of eight mice served as the input for single-cell sequencing studies, equalling 16 samples total. The capture and barcoding of single cells were performed across four separate experiments on 2 different days.

Per experiment, one littermate each of the genotypes *Cx3cr1*$^{+/-}$ and *Cx3cr1*$^{-/-}$ underwent unilateral whisker cauterization at P4, and their deprived and non-deprived cortices were then processed in parallel at P5, yielding 4 samples per experiment. A total of 3,000 cells were collected from each hemisphere of each mouse, equalling a total of ~48,000 cells collected overall. All libraries were prepared in parallel then pooled and sequenced together across two sequencing runs, as described below.

Generation of single-cell suspensions. Single-cell sequencing of mouse cortex using inDrops was performed as previously described[30]. Mice were transcardially perfused with ice-cold choline solution containing 2.1 g per liter $NaHCO_3$, 2.16 g per liter glucose, 0.172 g per liter NaH_2PO_4, 7.5 mM $MgCl_2$, 2.5 mM KCl, 10 mM HEPES, 15.36 g per liter choline chloride, 2.3 g per liter ascorbic acid, and 0.34 g per liter pyruvic acid (all chemicals from Sigma). A caveat of sequencing techniques that involve mechanical and enzymatic dissociation is that the dissociation process itself induces neural activity-dependent and injury-induced gene transcription. Therefore, because we were interested in analyzing sensory experience-dependent changes in gene expression across all cell types, a number of drugs that block neuronal activity and transcription were included in the perfusion solution. These included tetrodotoxin (1 µM; Sigma), 2-amino-5-phosphonopentanoic acid (AP-V, 100 µM; Thermo Fisher Scientific), actinomycin D (5 µg ml^{-1}; Sigma), and triptolide (10 µM; Sigma). Following 5 min of perfusion, deprived and non-deprived control somatosensory cortices were microdissected and each sample was transferred to a tube with 1.65 ml of preincubation solution containing HBSS (Life Technologies), 10 mM HEPES, 172 mg per liter kynurenic acid (Sigma) 0.86 g per liter $MgCl_2$, and 6.3 g per liter D-glucose (Sigma), pH 7.35, which was previously saturated with 95% O_2 and 5% CO_2 but was not bubbled after the sample was added. The drugs contained in the perfusion solution were also present in the preincubation solution at the same concentrations. After 30 min on ice, 1.65 ml of papain (Worthington) was added to a final concentration of 20 U ml^{-1}. Samples were moved to a rocker at 37 °C and gently rocked for 60 min.

Following the papain incubation at 37 °C, a series of triturations in increasingly small volumes were performed to fully dissociate the tissue. In between each round of trituration, the tissue was filtered through the corner of a 40-µM nylon cell strainer (Corning). The cells were then centrifuged at 300 × *g* for 5 min, and the pellet resuspended in 1 ml of trypsin inhibitor (Worthington) plus DNAse (Sigma) in preincubation solution without drugs (dissociation media, DM). The cells were washed by resuspension in DM adjusted to 0.04% BSA (Sigma) three times, then resuspended in DM containing 0.04% BSA and 15% Optiprep (Sigma) to a concentration of 100,000 cells per ml and transferred to the Single-Cell Core at Harvard Medical School for inDrops collection (see Acknowledgements).

Single-cell RNA-seq via inDrops. For each sample, ~3,000 cells were encapsulated into microfluidic droplets containing polyacrylamide gels with embedded barcoded reverse-transcription primers. Reverse transcription was carried out in intact droplets to generate barcoded cDNA from a single cell. Following droplet lysis, inDrops libraries were prepared as previously described[29,30]. All 16 libraries were indexed, pooled, and sequenced (read 1: 54 cycles; read 2: 21 cycles; index 1: 8 cycles; index 2: 8 cycles) across two runs on a NextSeq 500 (Illumina) with an average read depth across biological replicates of 8,815 reads per cell.

inDrops data processing. Sequenced reads were processed according to a previously published pipeline[60,61]. Briefly, this pipeline was used to build a custom transcriptome from Ensembl GRCm38 genome and GRCm38.84 annotation using Bowtie 1.1.1, after filtering the annotation gtf file (gencode.v17.annotation.gtf filtered for feature_type='gene', gene_type='protein_coding' and gene_status='KNOWN'). Read quality-control and mapping against this transcriptome were performed. Unique molecular identifiers (UMIs) were used to link sequence reads back to individual captured molecules. All steps of the pipeline were run using default parameters unless explicitly stated.

Quality control and clustering of cells. All cells were combined into a single dataset. Nuclei with >10% mitochondrial content were excluded from the dataset. Cells with fewer than 400 UMI counts were excluded. Cells were then clustered using the package Seurat R[62]. The data were log-normalized and scaled to 10,000 transcripts per cell. Variable genes were identified using the following parameters: x.low.cutoff = 0.0125, x.high.cutoff = 3, y.cutoff = 0.5. We limited the analysis to the top 30 principal components. Clustering resolution was set to 0.6. The expression of known marker genes was used to assign each cluster to one of the main cell types as follows: *Tubb3* and *Snap25* for neurons; *Gad1* and *Gad2* for inhibitory neurons; *Rorb* for excitatory cortical layer IV neurons; *Aldoc* and *Aqp4* for astrocytes; *Mbp* and *Plp1* for mature oligodendrocytes; *Pdgfra* and *Matn4* for immature oligodendrocytes; and *P2ry12* and *C1qa* for microglia. The analysis reported here focused on the glial population and layer IV neurons, for which the following numbers of cells per condition passed quality-control filters and were included in subsequent analyses. For cell numbers see Supplementary Fig. 9g.

Identification of differentially expressed genes. Differential gene expression analyses were performed in a pairwise fashion between each of the four groups using the R package Monocle2 (ref. [63]). The data were modeled using a negative binomial distribution consistent with data generated by high-throughput single-cell RNA-seq platforms such as inDrops. Unlike deep single-cell sequencing, inDrops probabilistically captures/samples the transcriptome of each cell and retrieves only a small fraction of all the present transcripts. Genes whose differential gene expression false discovery rate (FDR) was less than 0.10 (FDR < 0.10) were considered statistically significant.

Cell counts. For microglia cell counts, single-plane ×10 epifluorescence images were collected within the barrel cortex at the same exposure time with a Zeiss Observer microscope equipped with Zen Blue (Zeiss). Images of entire barrel fields from ×10 images were quantified blinded to the genotype in ImageJ (NIH). Each individual barrel per field of view was outlined and grouped as a single ROI. The same ROI was transposed to the thresholded microglia channel where the number of microglia in the barrels was quantified by counting the number of cells within the total barrel ROI. The entire perimeter of the barrel field was then outlined, and the number of microglia over the entire barrel field area was analyzed. The number of microglia within the septa was quantified by subtracting the total number of microglia within the barrels from the total number of microglia within the entire S1 ROI. The level of microglia infiltration into the barrel field was quantified by calculating the ratio of the total number of microglia in the barrels divided by the total number of microglia within the septa for each time point. Note that *Cx3cr1*$^{+/-}$ littermates were used for comparison to *Cx3cr1*$^{-/-}$ mice, as microglia within both sets of mice are labeled with EGFP and showed similar changes in TC synapses (Fig. 2). Similar results were obtained in wild-type mice in which microglia were labeled with Iba-1 (data not shown).

For ATF3$^+$, caspase 3$^+$, and APP$^+$ cell counts, single-plane ×20 (for trigeminal nerve ganglia) and single-plane ×10 (for thalamic VPM and primary somatosensory cortex) images were taken. The number of NeuN$^+$ and ATF3$^+$, caspase 3$^+$, or APP$^+$ cells for each plane was counted and divided by the total number of NeuN$^+$ cells and normalized to the total field of view area. For peripheral macrophage infiltration to the whisker follicles following cauterization, single-plane ×20 images were taken. The number of CX3CR1-EGFP$^+$ and CD45$^+$ cells within a given whisker follicle was counted and normalized to the total area of the whisker follicle.

In situ RNA hybridization. In situ RNA hybridization was performed according to the manufacturer's (ACDBio) specification with slight modifications. Briefly, mice were perfused with 4% PFA and brains were post-fixed for 24 h. Cryosections (10 µm) were prepared and stored at −80 °C. Before in situ hybridization, cryosections were equilibrated to room temperature for 1 h, then were dehydrated in a serial dilution of ethanol. Sections were incubated in hydrogen peroxide for 10 min and rinsed with RNase-free water. Sections were treated with Protease Plus for 15 min at room temperature and rinsed with PBS. In situ probes were added and incubated for 2 h at 40 °C. Subsequent amplification steps were performed according to the manufacturer's specification. Slices were immunostained following in situ hybridization. Sections were washed in 1× PBS for 10 min and blocked in 0.01% Triton X-100 and 2% normal goat serum for 30 min. Primary antibody (NeuN; Millipore) prepared in 0.01% Triton X-100 and 2% normal goat serum was added, and slides were incubated overnight at room temperature. Secondary antibody was prepared in 0.01% Triton X-100 and 2% normal goat serum and incubated at room temperature for 2 h. For *Cx3cl1* in situ quantification, the fluorescent RNA signal was localized to 4,6-diamidino-2-phenylindole (DAPI)$^+$ and NeuN$^+$ or DAPI$^-$ and NeuN$^-$ cells using a MATLAB script (custom script made in vR2016b, available upon request). Individual channels were segmented with a set threshold for dilating the masked signal around the NeuN$^+$ or DAPI$^+$ channels. For *Adam10* in situ quantification, the fluorescent RNA signal was colocalized to NeuN$^+$ or *Cx3cr1-EGFP*$^+$ cells, and the number of puncta colocalized to either signal was measured using Image J (NIH).

Structured illumination microscopy imaging. Immunostained sections were prepared as described above. Images were acquired on a GE Healthcare DeltaVision OMX microscope for structured illumination microscopy. Images were then processed in Imaris v.8.2.1 (Bitplane) to enable three-dimensional (3D) reconstruction of the cell and to visualize engulfed material.

Slice preparation and electrophysiological recordings. Male mice (~3 months old) were anesthetized by intraperitoneal injection of sodium pentobarbital (200 mg per kg) and then decapitated. The brain was quickly removed and placed in an oxygenated ice-cold cutting solution containing (in mM): 2.5 KCl, 1.25 NaH_2PO_4, 20 HEPES, 2 thiourea, 5 sodium-ascorbate, 92 NMDG, 30 $NaHCO_3$, 25 D-glucose, 0.5 $CaCl_2$, and 10 $MgSO_4$. Brain slices (200 µM) were made using a Leica VT1200 vibratome (Leica Biosystems). The brain slices were immediately transferred into an incubation chamber containing oxygenated cutting solution at 34 °C for 20 min. Slices were transferred into oxygenated artificial cerebrospinal fluid (ACSF) at room temperature (24 °C) for recording. ACSF solution contained (in mM): 125 NaCl, 2.5 KCl, 1.2 NaH_2PO_4, 1.2 $MgCl_2$, 2.4 $CaCl_2$, 26 $NaHCO_3$, and 11 D-glucose. Slices were left in this chamber for at least 1 h before being placed in a recording chamber at room temperature. Single slices were transferred into

a recording chamber continually superfused with oxygenated ACSF (30–32 °C) at a flow rate of ~2 ml min^{-1} for recording. Cells were visualized using infrared differential interference contrast (IR-DIC) imaging on an Olympus BX-50WI microscope. Electrophysiological recordings were recorded using an Axon Multiclamp 700B patch-clamp amplifier (Molecular Devices). sEPSCs were acquired in the whole-cell configuration and gap-free acquisition mode in Clampex (Axon Instruments). Neurons were held at a membrane potential of −70 mV. Signals were filtered at 1 kHz using the amplifier's four-pole, low-pass Bessel filter, digitized at 10 kHz with an Axon Digidata 1440A interface, and stored on a personal computer. Pipette solution contained (in mM): 120 K gluconate, 5 KCl, 2 $MgCl_2$, 10 HEPES, 4 ATP, 2 GTP. sEPSCs were recorded in the presence of bicuculline (20 µM) in the bath solution to block $GABA_A$ receptors. After recordings stabilized, 1-min duration of recording was taken for sEPSC analysis. sEPSC frequency and amplitude were detected using Mini Analysis Program (Synaptosoft). All recordings and quantification were performed blinded to conditions.

Pharmacological inhibition of ADAM10. C57BL/6J (fluorescence intensity analysis) or *Cx3cr1*$^{EGFP/+}$ (microglia engulfment analysis) mice were injected intraperitoneally every day with GI254023X (25 mg per kg; MilliporeSigma) following whisker cauterization at P4. The drug was prepared daily in 0.1 M carbonate buffer/10% dimethylsulfoxide vehicle. Control littermate animals were injected with vehicle following the same drug schedule for both fluorescence intensity and microglia engulfment analyses. Animals within each strain and within each litter were randomly assigned to either drug or vehicle treatment group.

Statistics and reproducibility. GraphPad Prism v.7.01 and v.5.01 provided the platform for all statistical and graphical analyses. All datasets were first tested and found to be normally distributed, and parametric statistics were subsequently run. Analyses included Student's *t*-test when comparing two conditions or two-way analysis of variance (ANOVA) followed by Sidak's, Tukey's, or Dunnett's post hoc analyses (indicated in the figure legends). For population data (percentage of cells expressing or binned data) a two-tailed Fisher's exact test or a Chi-square was used (indicated in the figure legends). All *P* and *n* values are specified within each figure legend. No statistical tests were used to predetermine sample sizes, but our sample sizes were similar to those reported in previous publications[2,7,29]. All images shown in figures are representative images of data quantified in corresponding graphs. For all whisker-deprivation experiments, each animal served as its own internal control, and relative changes were normalized to the spared, control hemisphere.

Reporting Summary. Further information on research design is available in the Nature Research Reporting Summary linked to this article.

Data availability

The data discussed in this publication have been deposited in the NCBI's Gene Expression Omnibus[64] and are accessible through GEO series accession number GSE129150. All tools, reagents, and data that support the findings will be shared on an unrestricted basis. All requests should be directed to the corresponding author.

References

50. Chozinski, T. J. et al. Expansion microscopy with conventional antibodies and fluorescent proteins. *Nat. Methods* **13**, 485 (2016).
51. Yang, C. et al. NRBF2 is involved in the autophagic degradation process of APP-CTFs in Alzheimer disease models. *Autophagy* **13**, 2028–2040 (2017).
52. Manabe, Y. et al. Glial cell line-derived neurotrophic factor protein prevents motor neuron loss of transgenic model mice for amyotrophic lateral sclerosis. *Neurol. Res.* **25**, 195–200 (2003).
53. Gey, M. et al. *Atf3* mutant mice show reduced axon regeneration and impaired regeneration-associated gene induction after peripheral nerve injury. *Open Biol.* **6**, 160091 (2016).
54. Hao, F. et al. Long-term protective effects of AAV9-mesencephalic astrocyte-derived neurotrophic factor gene transfer in parkinsonian rats. *Exp. Neurol.* **291**, 120–133 (2017).
55. Droguett, A. et al. Tubular overexpression of gremlin induces renal damage susceptibility in mice. *PLoS One* **9**, e101879 (2014).
56. Viganò, F. et al. GPR17 expressing NG2-glia: oligodendrocyte progenitors serving as a reserve pool after injury. *Glia* **64**, 287–299 (2016).
57. Kluge, M. G. et al. Age-dependent disturbances of neuronal and glial protein expression profiles in areas of secondary neurodegeneration post-stroke. *Neuroscience* **393**, 185–195 (2018).
58. Funk, K. E. & Klein, R. S. CSF1R antagonism limits local restimulation of antiviral CD8+ T cells during viral encephalitis. *J. Neuroinflamm.* **16**, 22 (2019).
59. Schafer, D. P., Lehrman, E. K., Heller, C. T. & Stevens, B. An engulfment assay: a protocol to assess interactions between CNS phagocytes and neurons. *J. Vis. Exp.* **88**, e51482 (2014).
60. Zilionis, R. et al. Single-cell barcoding and sequencing using droplet microfluidics. *Nat. Protoc.* **12**, 44–73 (2017).
61. Langmead, B., Trapnell, C., Pop, M. & Salzberg, S. L. Ultrafast and memory-efficient alignment of short DNA sequences to the human genome. *Genome Biol.* **10**, R25 (2009).
62. Satija, R., Farrell, J. A., Gennert, D., Schier, A. F. & Regev, A. Spatial reconstruction of single-cell gene expression data. *Nat. Biotechnol.* **33**, 495–502 (2015).
63. Trapnell, C. et al. The dynamics and regulators of cell fate decisions are revealed by pseudotemporal ordering of single cells. *Nat. Biotechnol.* **32**, 381–386 (2014).
64. Edgar, R., Domrachev, M. & Lash, A. E. Gene Expression Omnibus: NCBI gene expression and hybridization array data repository. *Nucleic Acids Res.* **30**, 207–210 (2002).

nature research

Corresponding author(s): Dorothy P. Schafer

Last updated by author(s): Apr 16, 2019

Reporting Summary

Nature Research wishes to improve the reproducibility of the work that we publish. This form provides structure for consistency and transparency in reporting. For further information on Nature Research policies, see Authors & Referees and the Editorial Policy Checklist.

Statistics

For all statistical analyses, confirm that the following items are present in the figure legend, table legend, main text, or Methods section.

n/a	Confirmed	
☐	☒	The exact sample size (*n*) for each experimental group/condition, given as a discrete number and unit of measurement
☐	☒	A statement on whether measurements were taken from distinct samples or whether the same sample was measured repeatedly
☐	☒	The statistical test(s) used AND whether they are one- or two-sided *Only common tests should be described solely by name; describe more complex techniques in the Methods section.*
☐	☒	A description of all covariates tested
☐	☒	A description of any assumptions or corrections, such as tests of normality and adjustment for multiple comparisons
☐	☒	A full description of the statistical parameters including central tendency (e.g. means) or other basic estimates (e.g. regression coefficient) AND variation (e.g. standard deviation) or associated estimates of uncertainty (e.g. confidence intervals)
☐	☒	For null hypothesis testing, the test statistic (e.g. *F*, *t*, *r*) with confidence intervals, effect sizes, degrees of freedom and *P* value noted *Give P values as exact values whenever suitable.*
☒	☐	For Bayesian analysis, information on the choice of priors and Markov chain Monte Carlo settings
☒	☐	For hierarchical and complex designs, identification of the appropriate level for tests and full reporting of outcomes
☒	☐	Estimates of effect sizes (e.g. Cohen's *d*, Pearson's *r*), indicating how they were calculated

Our web collection on statistics for biologists contains articles on many of the points above.

Software and code

Policy information about availability of computer code

Data collection	Microscopy: ZEN2 software (Zeiss) RNA/DNA quality: 2100 Expert Software BulkRNAseq: NextSeq System Suite, HiSeq Control Software, Illumina bcl2fastq2 Conversion Software v2.17 scRNAseq: Illumina basespace platform qPCR: BioRad CFX manager See also methods section.
Data analysis	Microscopy: Image J (NIH) and Imaris v 8.2.1 (Bitplane) Electrophysiology: Mini Analysis Program Single-cell RNAseq: inDrops.py (https://github.com/indrops/indrops), Bowtie 1.1.1, Monocle2 (RStudio) and MATLAB (v r2016b, Mathworks). Bulk RNA seq: TopHat2, HTSeq-count (v0.6.0), SPEctRA, DESeq2 package v.1.6.3, R (v3.1.1), Enrichr, Multiple Experiment Viewer 4.8, Ingenuity Pathway Analysis Graphs and statistics: Excel v.15.05101.1000 (Microsoft Office Professional Plus 2013) and Prism v7.01, v5.01 (Graphpad) See also methods section.

For manuscripts utilizing custom algorithms or software that are central to the research but not yet described in published literature, software must be made available to editors/reviewers. We strongly encourage code deposition in a community repository (e.g. GitHub). See the Nature Research guidelines for submitting code & software for further information.

Data

Policy information about availability of data

All manuscripts must include a data availability statement. This statement should provide the following information, where applicable:

- Accession codes, unique identifiers, or web links for publicly available datasets
- A list of figures that have associated raw data
- A description of any restrictions on data availability

All data that support the findings, tools, and reagents will be shared upon reasonable request. All requests should be directed to the corresponding author. All accession codes will be available after publication.

Field-specific reporting

Please select the one below that is the best fit for your research. If you are not sure, read the appropriate sections before making your selection.

☒ Life sciences ☐ Behavioural & social sciences ☐ Ecological, evolutionary & environmental sciences

For a reference copy of the document with all sections, see nature.com/documents/nr-reporting-summary-flat.pdf

Life sciences study design

All studies must disclose on these points even when the disclosure is negative.

Sample size	No statistical methods were used to pre-determine sample sizes but our sample sizes are similar to those reported in previous publications.
Data exclusions	No data points were excluded from our analyses.
Replication	Findings were replicated by three researchers within the lab (authors Gunner, G, Johnson, K and Lotun, A) and all attempts at replication were successful. All analyses were performed blind as described in our Methods.
Randomization	Both female and male littermate mice were used in our study with random allocation of males and females to each genotype and condition, described in our Methods.
Blinding	All analyses were performed blind; file names/animal IDs/genotypes were coded when performing our data analysis for fluorescence intensity, synapse density, and engulfment.

Reporting for specific materials, systems and methods

We require information from authors about some types of materials, experimental systems and methods used in many studies. Here, indicate whether each material, system or method listed is relevant to your study. If you are not sure if a list item applies to your research, read the appropriate section before selecting a response.

Materials & experimental systems

n/a	Involved in the study
☐	☒ Antibodies
☒	☐ Eukaryotic cell lines
☒	☐ Palaeontology
☐	☒ Animals and other organisms
☒	☐ Human research participants
☒	☐ Clinical data

Methods

n/a	Involved in the study
☒	☐ ChIP-seq
☒	☐ Flow cytometry
☒	☐ MRI-based neuroimaging

Antibodies

Antibodies used

anti-CD68 (1:1000; cat# MCA1957; lot# 1708; AbD Serotec; Raleigh, NC)
anti-VGluT2 (1:2000; cat# AB2251; lot# 3101508; MilliporeSigma; Darmstadt, Germany)
anti-Iba-1 (1:1000; cat# 019-18741; lot# PTR2404; Wako Chemicals; Richmond, VA)
anti-Homer1 (1:1000; cat# 160003; lot# 160003/1-47; Synaptic Systems; Goettingen, Germany)
anti-APP (1:1000; cat# 51-2700; lot# SA243371; ThermoFisher Scientific; Waltham, MA)
anti-Cleaved Caspase 3 (1:200; cat# 9661; lot# 45; Cell Signaling Technology; Danvers, MA)
anti-ATF3 (1:500; cat# HPA001562; lot# B116285; Sigma-Aldrich; Darmstadt, Germany)
Anti-NeuN (1:1000; cat# ABN91; lot# 3132967; MilliporeSigma; Darmstadt, Germany)
anti-CD45 (1:100; cat# MCA1388; lot# 170621; Bio-Rad; Hercules, CA)
anti- ALDH1L1 clone N103/39 (1:1000; cat# MABN495; lot# 2943620; MilliporeSigma; Darmstadt, Germany)
anti- NG2 (1:200; cat# AB5320; lot# 3061186; MilliporeSigma; Darmstadt, Germany)

anti- P2RY12 (1:100; cat# 848002; lot# B244070; Bio-Rad; Hercules, CA)
anti- F4/80 (1:1000; cat# MA-91124; lot# SJ2459832O; Invitrogen-ThermoFisher Scientific;Waltham, MA)
Goat anti-Chicken IgG (H+L) Secondary Antibody, Alexa Fluor 488 conjugate (1:1000; cat# A-11039; lot# 1937504; ThermoFisher Scientific; Waltham MA)
Goat anti-Rabbit IgG (H+L) Secondary Antibody, Alexa Fluor 488 conjugate (1:1000; cat# A-11034; lot# 1971418; ThermoFisher Scientific; Waltham MA)
Goat anti-Guinea Pig IgG (H+L) Secondary Antibody, Alexa Fluor 594 conjugate (1:1000; cat# A-11076; lot# 1848493; ThermoFisher Scientific; Waltham MA)
Goat anti-Rat IgG (H+L) Secondary Antibody, Alexa Fluor 594 conjugate (1:1000; cat# A-11007; lot# 1807719; ThermoFisher Scientific; Waltham MA)
Goat anti-Rabbit IgG (H+L) Secondary Antibody, Alexa Fluor 594 conjugate (1:1000; cat# A-11037; lot# 1205993; ThermoFisher Scientific; Waltham MA)
Goat anti-Rabbit IgG (H+L) Secondary Antibody, Alexa Fluor 647 conjugate (1:1000; cat# A-21245; lot# 2018272; ThermoFisher Scientific; Waltham MA)
Goat anti-Rat IgG (H+L) Secondary Antibody, Alexa Fluor 647 conjugate (1:1000; cat# A-21247; lot# 536061; ThermoFisher Scientific; Waltham MA)
Goat anti-Chicken IgG (H+L) Secondary Antibody, Alexa Fluor 647 conjugate (1:1000, cat# A-21449; lot# 1932506; ThermoFisher Scientific; Waltham MA)

Validation

Antibodies were selected according to the antibody validation profiles reported by the distributing companies and in publications:
anti- CD68 (species, Rat): This antibody cited by 45 publications on manufacturer's website. We have also previously validated that this marker is specific to microglia in the CNS and decreasing or increasing phagocytic rates also modulates CD68 levels (Schafer et al. Neuron 2012) further demonstrating specificity of this marker for lyosomal proteins. (Smith and Koch, Journal of Cell Science 1987 original antibody source).
anti- VGluT2 (species, Guinea Pig): previously published work shows specificity for labeling thalamocortical inputs (Nahmani and Erisir J Comp Neurol 2005) and for use in detecting layer IV TC inputs in the barrel cortex (Hoshiko et al J. Neurosci 2012).
anti- Iba1 (species, Rabbit): The use of this antibody is cited by 68 publications on manufacturer's website. We have also validated it labels microglia and macrophages with co-labeling with other markers in our current study and past studies (Schafer et al. Neuron 2012; Schafer et al. eLife 2016).
anti- Homer1 (species, Rabbit): cited by 13 publications on manufacturer's website for specificity to Homer-1 protein.
anti- APP (species, Rabbit): appears in 40 published figures according to manufacturer's website including 24 references for use in IHC.
anti- Cleaved Caspase 3 (species, Rabbit): cited by 3,479 publications on manufacturer's website.
anti- ATF3 (species, Rabbit): cited by 13 publications on manufacturer's website (KO validated by Gey et al Open Biol. Royal Society 2019). Additionally, ATF3 reactivity was tested on dorsal root ganglion tissue following a sciatic nerve injury in collaboration with C. Woolf lab (Harvard Medical School). Increased ATF3 reactivity was observed in injured dorsal root ganglion tissue in accordance with previous published reports on ATF3 reactivity following injury.
anti- NeuN (species, chicken): NeuN (RNA binding protein fox-1 homolog 3; Fox-1 homolog C) is a RNA-binding protein found exclusively in the nuclei of neuronal cells. It is a member of the evolutionarily conserved Fox-1 family and is mainly involved in splicing of RNA. From manufacturer's website: This Anti-NeuN Antibody is validated for use in IHC(P), Western Blotting, ICC for the detection of NeuN.
anti- CD45 (species, Rat): cited by 19 references on manufacturer's website for specificity to CD45 protein.
anti- ALDH1L1 clone N103/39 (species, Mouse): From manufacturer's website: Anti-Aldh1L1, clone N103/39 is an antibody targeting the Aldh1L1 protein, validated for use in Immunofluorescence, Immunohistochemistry, and Western Blotting.
anti- NG2 (species, Rabbit): From manufacturer's website: NG2 Chondroitin Sulfate Proteoglycan. AB5320 identifies both the intact proteoglycan and the core protein by Western blot and ELISA. When oligodendrocyte precursor cells (i.e. O-2A progenitor cells) are stained alive, the stain appears as clusters on the cell surface. This antibody does not stain differentiated oligodendrocytes well.
anti- P2RY12 (species, Rabbit): From manufacturer's website: Each lot of this antibody is quality control tested by formalin-fixed paraffin-embedded immunohistochemical staining. For immunohistochemistry, a concentration range of 5.0 - 10 µg/ml is suggested. 1 publication cited on manufacturer's website.
anti- F4/80 (species, Rat): references by 29 publications according to manufacturer's website for specificity to F4/80. From website: MA1-91124 has been successfully used in immunohistochemistry (frozen tissue), immunohistochemistry (paraffin tissue), immunoprecipitation, Western blot, radioimmune assay and Flow cytometry applications.

Animals and other organisms

Policy information about studies involving animals; ARRIVE guidelines recommended for reporting animal research

Laboratory animals

SERT-Cre mice were a generous gift from Dr. Mark Ansorage, Columbia University and provided by Dr. Sacha Nelson, Brandeis University. Cx3cl1-/- mice were provided by Dr. Sergio Lira (Ichan School of Medicine, Mount Sinai). Rosa26-TdTomato mice (Ai14; stock #007914), Cx3cr1-/- mice (Cx3cr1EGFP/EGFP; stock #005582), CR3-KO mice (stock #003991), and C57Bl6/J (stock #000664) mice were obtained from Jackson Laboratories (Bar Harbor, ME). Heterozygous breeder pairs were set up for all experiments and wild-type and heterozygote littermates were used as controls with equal representation of males and females for each genotype unless otherwise specified in figure legends. Mice were cauterized at postnatal day 4 (P4) for all whisker lesioning and whisker trimming experiments and sacrificed at various ages including P5, P6, P7, P8, P9, P10, P11, P21, and P90. See main text and figure legends for specific ages used in each experiment.

Wild animals

No wild animals were used in this study.

Field-collected samples

No field-collected samples were used in this study.

Ethics oversight	All experiments were performed in accordance with animal care and use committees (UMass Medical School IACUC) and under NIH guidelines for proper animal welfare.

Note that full information on the approval of the study protocol must also be provided in the manuscript.